


Viscous free-surface flows past cylinders

Edward M. Hinton *

*Bullard Laboratories, University of Cambridge, Madingley Road,
Cambridge, CB3 0EZ, United Kingdom*

Andrew J. Hogg 

*School of Mathematics, University of Bristol, Woodland Road, Bristol,
BS8 1UG, United Kingdom*

Herbert E. Huppert

*Institute of Theoretical Geophysics, King's College, University of Cambridge,
Cambridge, CB2 1ST, United Kingdom*



(Received 29 July 2019; accepted 17 July 2020; published 4 August 2020)

Free-surface flows of viscous liquid down an inclined plane and past cylinders of various cross-sections are investigated theoretically and experimentally. The cylinders are oriented with their axis perpendicular to the plane and are sufficiently tall that they are not overtopped. A lubrication model is applied to derive the steady governing equation for the flow depth, which is integrated numerically and analyzed asymptotically to calculate how the depth of a steady uniform flow is perturbed as it flows past the cylinder. Flows past cylinders that are narrow relative to the depth of the oncoming flow are only slightly perturbed, but for relatively wide cylinders, there forms a pond of nearly stationary fluid upstream of the cylinder and a dry region in which there is no fluid downstream of the cylinder. The structure of the flow in the regime of a relatively wide cylinder depends in detail upon the curvature of the cylinder at the upstream stagnation point. For flows past cylinders with circular and square cross-sections, the maximum flow depth occurs at the upstream stagnation point. Its numerical value may be predicted analytically on the basis of the asymptotic expressions and exhibits different dependencies upon the variables that characterize the motion. In addition, wedge-shaped obstructions are analyzed for which the flow depth increases along the wedge wall and the maximum flow depth occurs away from the upstream stagnation point. The results from new laboratory experiments of flows past circular cylinders are reported and these corroborate the theory, confirming the occurrence of both pond and dry regions. The investigation has direct relevance to the deflection of lava flows by barriers and buildings and the theory is employed to deduce simplified asymptotic expressions of the force exerted on the cylinders.

DOI: [10.1103/PhysRevFluids.5.084101](https://doi.org/10.1103/PhysRevFluids.5.084101)

I. INTRODUCTION

The interaction between a free-surface viscous flow and immobile obstructions on an inclined plane occurs in many industrial and environmental contexts. It is often important to quantify the stress that is exerted on an obstruction and determine how the free surface is perturbed. These flows are dominated by different forces depending on the lengthscale and shape of the obstruction, and

*edward@bpi.cam.ac.uk

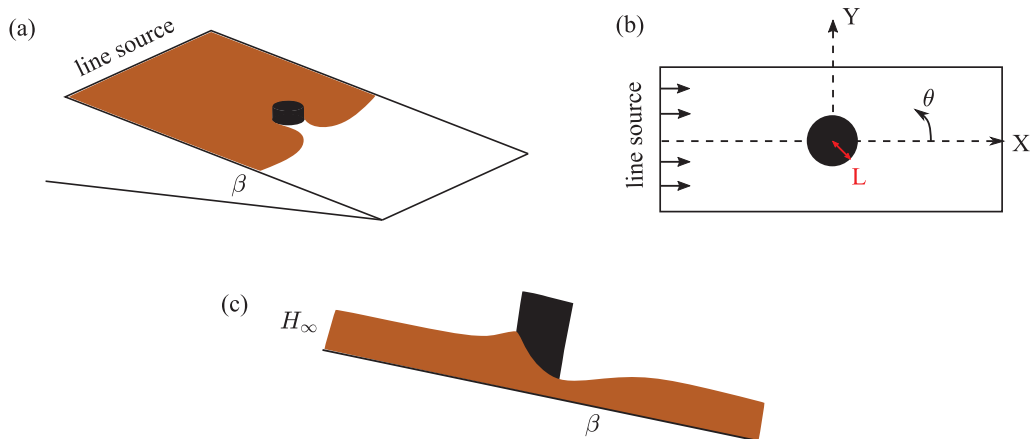


FIG. 1. (a) Schematic for viscous flow down an inclined plane at an angle, β , to the horizontal, past a cylinder from a line source. (b) Plan view of the setup. The cylinder has radius L , the X axis is in the direction of steepest descent and the Y axis is in the cross-slope direction. (c) Side view of the flow showing the flow thickness far upstream, H_∞ , and the perturbation owing to the cylinder.

the properties of the fluid. A common feature in many applications is that the flow is thin relative to the longitudinal lengthscale and so the lubrication approximation may be applied [1].

There has been extensive theoretical and numerical research on thin-film flows over adhered obstacles, for which surface tension plays a key role [2–5]. These studies have important applications in manufacturing and printing owing to the ubiquity of coating flows in such industries. The role of surface tension in thin-film flows past cylinders has been investigated numerically [6,7], while capillary effects on viscously dominated flows around isolated and periodic obstructions have also been analyzed [8–12]. In addition to surface tension, inertia may be significant in some interactions between thin films and obstructions [13,14]. Significant progress has also been made in the inverse problem; determining the underlying topography given a known free surface, which is important for determining the required bottom topography for a desired free-surface profile [15,16].

For viscous flow past large obstructions, the flow may not coat the obstruction and in this case there are dry regions in which there is no liquid. Some studies have determined when an obstruction will lead to a dry region rather than the obstruction being surmounted by the flow [17,18]. Dry regions may also arise owing to instabilities associated with surface tension effects, particularly when the film is very thin [19–25]. Yatim *et al.* [26] showed that in the absence of any capillary effects or obstructions to the flow, a dry region, which may develop for example owing to isolated heating, has parabolic shape and migrates steadily downslope.

In the present study, we analyze the interaction of free-surface viscous flow with cylindrical obstructions that are oriented with their axis perpendicular to the inclined plane and which are of a sufficient height that the flow does not surmount them (see Fig. 1). The motivation of the work is, in part, to inform the construction of barriers used to divert volcanic lava flows, which can cause enormous damage to homes and infrastructure [27].

Lava is a complex liquid with a rheology that can change rapidly and it solidifies at its boundaries to form crust [28,29]. Modeling lava as a Newtonian viscous liquid has nevertheless proved useful and accurate in many contexts [30,31] and we adopt this view in the present work. We also neglect surface tension because it is insignificant at the relatively large scales of interest, potentially apart from very close to the contact line.

The motion of a viscous Newtonian liquid down an inclined plane from either point or line sources has been widely researched; in particular it has been shown that a steady flow arises from

a line source delivering a constant volume flux of liquid per unit width [32–34]. The interaction of this steady flow with a topographical mound was the subject of a previous paper [18]. It was shown, and analyzed quantitatively, that smaller mounds are surmounted by the flow while taller mounds lead to dry regions in which there is no liquid and a build up of liquid in a pond upstream of the mound (see also the investigation of the lava field at Marcath volcano, [35]).

The present work, investigating the interaction of a downslope viscous flow with cylindrical obstructions, pertains to lava barriers that are steeper and taller than those considered in Ref. [18]. Such barriers were proposed in Hawaii to protect a research observatory [36] and in part motivated by this plan, laboratory experiments investigating the influence of perpendicular obstructions were carried out by Dietterich *et al.* [37]. Interesting research results have been established for the related problem of the deflection of rapid downslope granular flows by obstructions, which is important for the construction of avalanche defenses [38–40]. For these inertially controlled flows, there are now guidelines for the design of defense schemes [41]; we note there is no equivalent guidance for viscously-controlled lava flows.

Additionally, the present work has important applications to the study of the interaction between lava and trees. As an example, observations of ‘lava-trees’ post-eruption may be used to determine properties of the lava flow [42]. It has been shown that forests slow the advance of a lava flow and lead to build up of lava upstream [43]. Our results demonstrate similar phenomena.

Free-surface flows are often modeled mathematically by strongly nonlinear partial differential equations and many of the research results described above came through numerical computation, coupled to experimental investigations (for a review, see [14]). In this study, we employ both of these approaches. However, in addition, we derive asymptotic results that show good agreement with our computational results and yield both a simplified quantification of the flow depth and insight into the interplay of the dominant physical processes. Since part of the aim of the present paper is to inform barrier construction, we quantify how the flow depth increases upstream of a cylinder to determine how tall an obstruction must be to prevent overtopping; we also make estimates of the force exerted on the obstruction. The results are calculated numerically and through explicit analytical expressions that result from our asymptotic analysis.

The paper is structured as follows. In Sec. II, we formulate the lubrication model for a free-surface viscous flow past a cylindrical obstruction, following Sec. 2 of Hinton *et al.* [18]. We identify a single parameter, \mathcal{F} , which is a dimensionless proxy for the upstream flow depth relative to the width of the cylinder. We then present a numerical scheme and results for the steady flow depth. These demonstrate that for sufficiently wide cylinders ($\mathcal{F} \ll 1$), the depth increases significantly upstream of the cylinder and there are dry regions with no liquid downstream of the cylinder. For relatively narrow cylinders ($\mathcal{F} \gg 1$), the perturbation to the upstream flow depth is small.

In Sec. IV, we determine an asymptotic approximation for the case of flows past a relatively narrow circular cylinder, corresponding to the regime $\mathcal{F} \gg 1$. In Sec. V, we consider the other regime of a relatively wide cylinder ($\mathcal{F} \ll 1$) and show that the depth increases by a factor proportional to $\mathcal{F}^{-1/4}$ to leading order. Laboratory experiments are presented in Sec. VI and these corroborate our theory. Finally, in the last two sections, we study how the flow is perturbed upstream of a relatively wide square cylinder [Sec. (VII)] and a relatively wide wedge [Sec. (VIII)]. The three shapes of cylinder analyzed in this study (Secs. V, VII, and VIII) exhibit different behavior and dependencies of the upstream flow depth upon the properties of the flow (represented through the dimensionless parameter \mathcal{F}). This is associated with the different curvatures at the stagnation point; for a circle the curvature is finite, for a square it vanishes, while a wedge has infinite curvature at the vertex.

This paper also includes three appendices (A, B, and C), which include algebraic details of some of the asymptotic analyses. They are important to establish completely the behavior of the dependent variables in the asymptotic regimes, but are presented in appendices to not detract from the exposition of the main results.

II. FORMULATION

We analyze the free-surface flow of a liquid of dynamic viscosity μ down a rigid inclined plane at an angle β to the horizontal (Fig. 1). We denote the downslope coordinate by X , the cross-slope coordinate by Y and the normal distance above the inclined plane by Z . Throughout this paper, we focus on the steady solution that develops long after the current first passes the obstruction. The steady depth of the liquid is given by $H(X, Y)$. We assume that the liquid is sufficiently viscous that the effects of both inertia and surface tension can be neglected (i.e. the Reynolds number is sufficiently small and the capillary number is sufficiently large). These assumptions are explicitly quantified when we describe our experiments (Sec. VI).

We further assume that the flow is “shallow,” meaning that its thickness, H , is much smaller than its characteristic lengthscale, L , parallel to the inclined plane. Continuity imposes that the component of velocity normal to the plane, W , is much smaller than the velocities in the X and Y directions by a factor of H/L . This simplification, known as lubrication theory, applies to many gravity-driven and pressure-driven viscous flows and flows in porous media [33,44–46]. The flow is assumed to be predominantly parallel to the inclined plane and the pressure within the liquid is hydrostatic to leading order [1].

One limitation of lubrication theory is that a retreating contact line cannot occur, for example at the upstream edge of a fixed volume of liquid flowing over inclined plane [33]. Instead, the theory suggests that receding regions are very slowly draining thin films. For the problem considered presently, this limitation is unimportant because dry regions can occur only in a region downstream of the cylinder into which liquid never flows, thus the contact line is nowhere receding.

Following Lister [33], we derive the flow velocities in the X and Y directions and then from local mass conservation obtain the steady nonlinear partial differential equation governing H (first derived by Nusselt [47]),

$$\frac{\partial}{\partial X} \left[\left(\sin \beta - \frac{\partial H}{\partial X} \cos \beta \right) H^3 \right] - \frac{\partial}{\partial Y} \left[\frac{\partial H}{\partial Y} H^3 \cos \beta \right] = 0. \quad (1)$$

We consider the motion arising from a line-source supplying a constant flux Q per unit width far upstream [$X \rightarrow -\infty$; see Fig. 1(a)]. The steady flow advances with constant depth, given by [1,33,47]

$$H_\infty = \left(\frac{3\mu Q}{\Delta\rho g \sin \beta} \right)^{1/3}, \quad (2)$$

where g is the gravitational acceleration and $\Delta\rho$ is the density difference between the liquid and air, essentially the liquid density. We consider the interaction between this flow and obstructions with lengthscale, L , measured parallel to the inclined plane (for example, a circular cylinder of radius L , see Fig. 1). We assume that the channel is much wider than the obstruction so that it may be considered isolated and we reiterate that we have used the lubrication approximation, which is equivalent to assuming $H_\infty/L \ll 1$.

We restrict our attention to cylindrical obstructions that are sufficiently high that they pierce the free surface and there is no overtopping during the ensuing motion. The overtopping of topographical mounds was part of the consideration of Ref. [18]. We introduce the following dimensionless variables:

$$x = X/L, \quad y = Y/L, \quad h = H/H_\infty. \quad (3)$$

Using Eq. (1), we find the following governing equation for the steady dimensionless depth, $h(x, y)$,

$$\frac{\partial h^3}{\partial x} = \mathcal{F} \left[\frac{\partial}{\partial x} \left(h^3 \frac{\partial h}{\partial x} \right) + \frac{\partial}{\partial y} \left(h^3 \frac{\partial h}{\partial y} \right) \right], \quad (4)$$

where the dimensionless parameter,

$$\mathcal{F} = \frac{H_\infty}{L \tan \beta} = \left[\frac{3\mu Q}{(\Delta\rho g \sin \beta)L^3 \tan^3 \beta} \right]^{1/3}, \quad (5)$$

is the ratio of downslope to lateral pressure gradients. It quantifies the importance of the diffusive terms on the right-hand side of Eq. (4), associated with the gravity-driven slumping of the liquid, relative to the downslope advective term on the left-hand side of Eq. (4), associated with the gravity-driven flow down the plane. The dimensionless velocity is given by

$$\mathbf{u} = \frac{3}{2}z(2h - z) \left(1 - \mathcal{F} \frac{\partial h}{\partial x}, -\mathcal{F} \frac{\partial h}{\partial y} \right). \quad (6)$$

This parabolic velocity profile is typical of flows governed by a simple balance between viscous stresses and a uniform driving force (in this case gravity).

We begin the analysis by considering circular cylinders of radius L , centered on the origin. In dimensionless polar coordinates, with $x = r \cos \theta$, $y = r \sin \theta$ and the cylinder lies within $r < 1$, the steady governing equation for the motion ($r > 1$) is given by

$$\cos \theta \frac{\partial h^3}{\partial r} - \frac{\sin \theta}{r} \frac{\partial h^3}{\partial \theta} = \frac{1}{4} \mathcal{F} \nabla^2 h^4. \quad (7)$$

In this coordinate system the components of the velocity in the radial and azimuthal directions are

$$u_r = \frac{3}{2}z(2h - z) \left[\cos \theta - \mathcal{F} \frac{\partial h}{\partial r} \right], \quad (8)$$

$$u_\theta = \frac{3}{2}z(2h - z) \left[-\sin \theta - \frac{\mathcal{F}}{r} \frac{\partial h}{\partial \theta} \right], \quad (9)$$

respectively. We impose a no-flux boundary condition at the edge of the obstruction, $\mathbf{u} \cdot \mathbf{n} = 0$, where \mathbf{n} is the outward pointing normal, which becomes

$$h^3 \left(\mathcal{F} \frac{\partial h}{\partial r} - \cos \theta \right) = 0 \quad \text{on} \quad r = 1. \quad (10)$$

We require that the flow depth returns to its unperturbed value far from the cylinder,

$$h \rightarrow 1 \quad \text{as} \quad r \rightarrow \infty. \quad (11)$$

Finally, we allow free-slip on the obstruction in accordance with the leading-order lubrication model. Under our assumption of shallow flow ($H_\infty/L \ll 1$), the X and Y viscous stress terms, $\mu \partial^2 U / \partial X^2$ and $\mu \partial^2 U / \partial Y^2$ are neglected in the momentum equation. The order of the problem is therefore reduced and the no-slip boundary condition on the cylinder cannot be imposed. There is a region localised to the cylinder where the second order X and Y derivatives of the velocity become important. Our model neglects this region, which has been shown to occupy $R - L \sim H_\infty$ (for a detailed analysis of the inner region and the matching with the outer lubrication flow, see [48,49]). In addition, if small inertial terms are reintroduced into the problem then the perpendicular component of the velocity is nonzero in this region and there are secondary flows associated with the no-slip boundary, which we also neglect [48–51]. We show that the region in which no-slip is important is smaller than the “inner” regions of the asymptotic analysis of our lubrication model in both the regime $\mathcal{F} \gg 1$ (Sec. IV) and the regime $\mathcal{F} \ll 1$ (Sec. V). Henceforth, we neglect the effects of no-slip on the cylinder wall.

III. NUMERICAL METHOD

We used MATLAB’s Partial Differential Equation Toolbox to solve the steady governing Eq. (7). A similar approach was used in Hinton *et al.* [18] for flow over a mound. The program uses

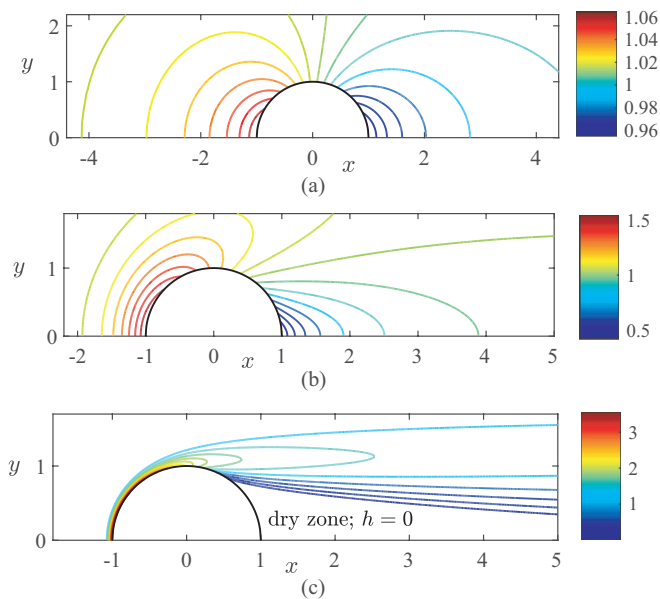


FIG. 2. Contour plot of the thickness of the steady flow past a cylinder with dimensionless radius $r = 1$ for three values of the flow parameter, \mathcal{F} . (a) $\mathcal{F} = 20$ (diffusive terms dominate advective terms), (b) $\mathcal{F} = 1$ (diffusive terms and advective terms are comparable and both are important), and (c) $\mathcal{F} = 0.025$ (advective terms dominate the diffusive terms).

numerical finite elements to compute the solution. The steady state is found iteratively; we take an initial guess to be $h = 1$ everywhere, corresponding to flow without an obstruction and iterate until a converged solution is found. The toolbox performs adaptive two-dimensional mesh generation and refinement to determine the influence of the cylinder.

We solve the governing equation on the domain $0 < y < c$, $a < x < b$ (where $a < 0$), with the unit semicircle in $y > 0$, centered at the origin, removed [see Fig. 2(a)]. Since the problem is symmetric about the centerline $y = 0$ we solve the governing equation only in $y \geq 0$ to reduce computational effort.

The boundary conditions on the domain are as follows. The upstream line source supplies constant flux; thus $h(x = a) = 1$. Symmetry requires that $\partial h / \partial y = 0$ on the centerline $y = 0$. We impose a no-flux condition into the cylinder boundary, which is given by Eq. (10). We impose the far-field condition Eq. (11), $h = 1$, on the other boundaries ($y = c$ and $x = b$). For each value of \mathcal{F} , we run our numerical technique on an initial domain and subsequently increase the domain size until the results become independent of further increases to it. For example, with $\mathcal{F} = 0.1$, we used $a = -4$, $b = 40$, and $c = 5$. Typically, we use approximately 100 000 elements to provide sufficient resolution. Contour plots of the thickness of the flow for three values of \mathcal{F} are shown in Fig. 2.

For large \mathcal{F} , the diffusive terms in the governing Eq. (7) dominate and the perturbation to the flow depth due to the cylinder is small, as illustrated in Fig. 2(a). The minimum thickness of the current (at $x = 1$, $y = 0$) decreases as \mathcal{F} is decreased, corresponding to a relatively wider cylinder, steeper slope or shallower current (or a combination of these). For $\mathcal{F} = 1$, the minimum thickness is approximately half of the flow thickness found far upstream [Fig. 2(b)]. For sufficiently small \mathcal{F} , dry zones in which the flow depth vanishes ($h = 0$) can occur [see Fig. 2(c)].

The original numerical scheme was not effective when there were dry regions because the diffusive term is degenerate as $h \rightarrow 0$. We note that this is not a limitation of lubrication theory because the dry region is never invaded by the liquid so it is not a draining film. To overcome the degeneracy, we introduced a small source at the downstream edge of the cylinder, $r = 1$,

$0 < \theta < \pi/2$, to provide a “virtual” thin film over the dry region. It is analogous to radially “squirting” a very small amount of liquid from the cylinder. The boundary condition on the cylinder Eq. (10) is then adjusted to

$$h^3 \left(\cos \theta - \mathcal{F} \frac{\partial h}{\partial r} \right) = \epsilon \quad \text{on } r = 1, \quad 0 < \theta < \pi/2. \quad (12)$$

The magnitude of the source, ϵ , was minimized subject to the constraint that the thin film coats the dry region (and consequently the thickness of the flow everywhere satisfies $h > 0$). At such values of ϵ , the flow thickness becomes independent of ϵ away from the dry zone. Typically, we use $\epsilon = 10^{-6}$. The edge of the dry region can be determined by analyzing where the flow thickness steeply increases from its approximately constant value in the thin film.

We computed the flow thickness for a wide range of values of the parameter, $0.025 \leq \mathcal{F} \leq 40$. In the following sections, we use asymptotic analysis to interpret the results.

IV. FLOW PAST A NARROW CIRCULAR CYLINDER ($\mathcal{F} \gg 1$)

We first comment that the regime $\mathcal{F} \gg 1$ is consistent with the lubrication approximation, $H_\infty/L \ll 1$, provided that

$$\tan \beta \ll H_\infty/L \ll 1. \quad (13)$$

For $\mathcal{F} \gg 1$, the flow remains attached to the cylinder, i.e., there are no dry regions downstream. The increase in depth upstream of the cylinder is small relative to the far upstream depth [see Fig. 2(a)]. This motivates seeking an expansion for h in the case $\mathcal{F} \gg 1$, about the far-field depth, $h = 1$, of the form

$$h = 1 + \mathcal{F}^{-1}h_1 + \mathcal{F}^{-2}h_2 + \dots \quad (14)$$

At $\mathcal{O}(1)$, Eq. (7) is

$$\nabla^2 h_1 = 0, \quad (15)$$

subject to boundary conditions Eqs. (10) and (11),

$$\frac{\partial h_1}{\partial r} = \cos \theta \quad \text{at } r = 1, \quad (16a)$$

$$h_1 \rightarrow 0 \quad \text{as } r \rightarrow \infty. \quad (16b)$$

We seek a separable solution in r and θ , which satisfies the boundary conditions and obtain

$$h_1 = -r^{-1} \cos \theta. \quad (17)$$

At $\mathcal{O}(\mathcal{F}^{-1})$, Eq. (7) is

$$\nabla^2 h_2 = 3 \cos \theta \frac{\partial h_1}{\partial r} - 3 \frac{\sin \theta}{r} \frac{\partial h_1}{\partial \theta} - \frac{3}{2} \nabla^2 h_1^2. \quad (18)$$

We substitute our expression Eq. (17) for h_1 , which yields

$$\nabla^2 h_2 = 3r^{-2} \cos 2\theta - 3r^{-4}. \quad (19)$$

The boundary conditions for h_2 are

$$\frac{\partial h_2}{\partial r} = 0 \quad \text{at } r = 1, \quad (20a)$$

$$h_2 \rightarrow 0 \quad \text{as } r \rightarrow \infty. \quad (20b)$$

The general solution to Eq. (19) is

$$h_2 = A_0 \log(r) + B_0 + \sum_{n=1}^{\infty} (A_n r^n + B_n r^{-n}) [C_n \cos n\theta + D_n \sin n\theta] - \frac{3}{4} \cos 2\theta - \frac{3}{4} r^{-2}, \quad (21)$$

where A_n , B_n , C_n , and D_n are constants to be determined. The last two terms represent the complementary function arising from the right-hand side of Eq. (19). We impose $A_n = 0$ (for $n \geq 1$) because h_2 cannot grow algebraically in the far-field if it is to match with $h_2 \rightarrow 0$ as $r \rightarrow \infty$. Applying the boundary condition at $r = 1$ [Eq. (20a)], we find $A_0 = -3/2$ and $B_n = 0$ (for $n \geq 1$) and obtain

$$h_2 = -\frac{3}{2} \log(r) + B_0 - \frac{3}{4} \cos 2\theta - \frac{3}{4} r^{-2}. \quad (22)$$

It is not possible to apply the boundary condition as $r \rightarrow \infty$ [Eq. (20b)], because $A_0 \neq 0$ and hence $h_2 \sim \log r$.

Instead, in the regime $\mathcal{F} \gg 1$, the solution forms two asymptotic regions close to and far from the cylinder. When the radial distance is $\mathcal{O}(\mathcal{F})$, the advective terms, on the left-hand side of Eq. (7), are comparable with the diffusive terms. The problem is therefore singular and its asymptotic approximation comprises an ‘‘inner’’ region close to the cylinder which is matched to an ‘outer’ region far from it (for further details of this general idea, see Chapter 5 of Ref. [52]). There is an analogy here with the resolution of the Whitehead paradox for low Reynolds number flow past a sphere, resolved by Proudman and Pearson [53], where an outer region is introduced to account for inertial effects. The regular expansion for flow past a sphere is accurate to leading order, but matching is required at next order.

Next, we seek an asymptotic expansion for the depth in the outer region where the advective and diffusive terms balance.

A. Outer region

The distinguished limit for the outer region of Eq. (7) occurs when we rescale r with \mathcal{F} by

$$r = \mathcal{F} \hat{r}, \quad (23)$$

where \hat{r} is order 1, and we define $\hat{x} = \hat{r} \cos \theta$ and $\hat{y} = \hat{r} \sin \theta$. The governing Eq. (7) in the rescaled coordinates is

$$\frac{\partial h^3}{\partial \hat{x}} = \left[\frac{\partial}{\partial \hat{x}} \left(h^3 \frac{\partial h}{\partial \hat{x}} \right) + \frac{\partial}{\partial \hat{y}} \left(h^3 \frac{\partial h}{\partial \hat{y}} \right) \right]. \quad (24)$$

Since $h \rightarrow 1$ as $\hat{r} \rightarrow \infty$, we seek an outer expansion of the form $h = 1 + \delta(\mathcal{F}) \hat{h}$, where $\delta(\mathcal{F}) \ll 1$ is to be determined as part of the matching procedure. The leading-order equation for \hat{h} is

$$3 \frac{\partial \hat{h}}{\partial \hat{x}} = \nabla^2 \hat{h}, \quad (25)$$

which is linear. By letting $\hat{h} = \phi(\hat{r}, \theta) e^{3\hat{x}/2}$, Eq. (25) is transformed into a more familiar equation for $\phi(\hat{r}, \theta)$ (see chapter 5 of Ref. [52]):

$$(\nabla^2 - 9/4)\phi = 0. \quad (26)$$

Note that the boundary condition in the far field for ϕ is that it decays faster than $e^{-3\hat{x}/2}$ in order that $\hat{h} \rightarrow 0$ as $\hat{r} \rightarrow \infty$. Equation (26) has separable solutions of the form

$$\phi = [a_m \cos(m\theta) + b_m \sin(m\theta)] \Phi(\hat{r}), \quad (27)$$

where a_m and b_m are constants and Φ satisfies

$$\hat{r}^2 \Phi'' + \hat{r} \Phi' - (9/4) \hat{r}^2 \Phi - m^2 \Phi = 0. \quad (28)$$

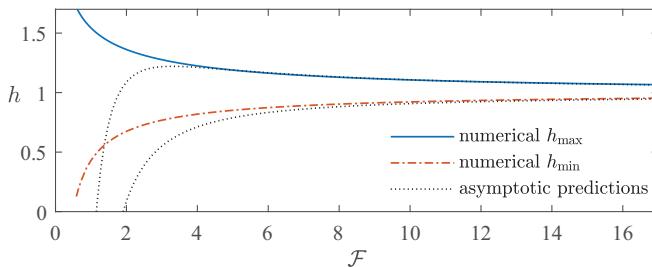


FIG. 3. The maximum (blue solid line) and minimum (red solid line) depths, calculated from our numerical technique, for steady flow past a cylinder as functions of the parameter \mathcal{F} . The deepest point is always at the stagnation point on the upstream boundary at $\theta = \pi$, while the shallowest point is on the downstream boundary at $\theta = 0$. The asymptotic predictions for the two extrema, calculated from Eq. (33), are plotted as black dotted lines, which show good agreement for $\mathcal{F} \gg 1$,

The general solution for Φ is

$$\Phi = c_m I_m(3\hat{r}/2) + d_m K_m(3\hat{r}/2), \quad (29)$$

where I_m and K_m are modified Bessel functions of the first and second kind, respectively [54], and c_m and d_m are constants. The function I_m grows as $\hat{r} \rightarrow \infty$, which imposes $c_m = 0$. We note that for $\hat{r} \gg 1$

$$K_m(3\hat{r}/2) \sim \sqrt{\frac{\pi}{3\hat{r}}} e^{-3\hat{r}/2}, \quad (30)$$

which implies that $\hat{h} \sim \hat{r}^{-1/2} \rightarrow 0$ as $\hat{r} \rightarrow \infty$, as required. Finally, since the flow is symmetric about the x axis, the coefficients of the $\sin(m\theta)$ terms in Eq. (27) vanish; $b_m = 0$. Putting this together, we obtain the following expression for the outer expansion

$$h = 1 + \delta(\mathcal{F})\hat{h} = 1 + \delta(\mathcal{F}) \sum_{m=0}^{\infty} a_m \cos(m\theta) K_m(3\hat{r}/2) e^{3\hat{x}/2}. \quad (31)$$

The remaining undetermined constants occurring in the inner and outer expansion are obtained by matching, the details of which are given in Appendix A. We find that the outer expansion is

$$h = 1 + (3/2)\mathcal{F}^{-2} [K_0(3\hat{r}/2) - \cos\theta K_1(3\hat{r}/2)] e^{(3\hat{r}\cos\theta)/2}, \quad (32)$$

and the inner expansion is

$$h = 1 - \frac{\cos(\theta)}{\mathcal{F}r} - \frac{3}{4\mathcal{F}^2} \left[2 \log\left(\frac{3r}{4\mathcal{F}}\right) + 2\gamma + 2 \cos^2(\theta) + r^{-2} \right], \quad (33)$$

where $\gamma \approx 0.577$ is the Euler constant. We use Eq. (33) to evaluate the flow depth attained on the cylinder ($r = 1$) at the upstream stagnation point ($\theta = \pi$) and the downstream point ($\theta = 0$), which give the maximum and minimum perturbations to the depth of the flow, respectively, in the regime $\mathcal{F} \gg 1$,

$$h_{\max} = h(1, \pi) = 1 + \frac{1}{\mathcal{F}} - \frac{3}{4\mathcal{F}^2} \left[2 \log\left(\frac{3}{4\mathcal{F}}\right) + 2\gamma + 3 \right], \quad (34)$$

$$h_{\min} = h(1, 0) = 1 - \frac{1}{\mathcal{F}} - \frac{3}{4\mathcal{F}^2} \left[2 \log\left(\frac{3}{4\mathcal{F}}\right) + 2\gamma + 3 \right]. \quad (35)$$

In Fig. 3, we compare these predictions with the maximum and minimum flow thicknesses from the numerical solution of the governing Eq. (7). There is excellent agreement in the regime $\mathcal{F} \gg 1$.

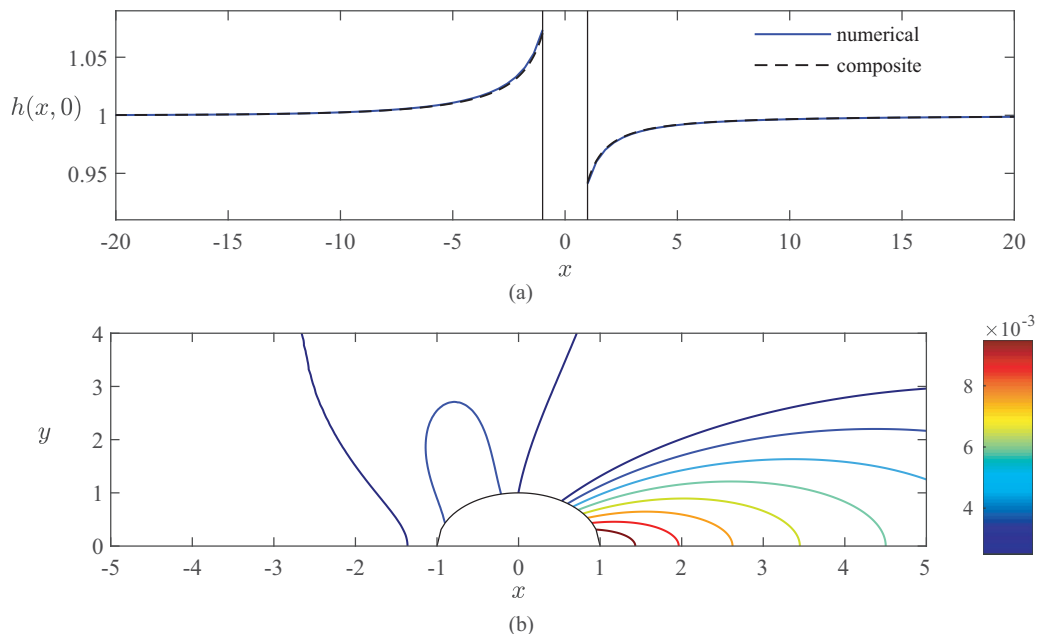


FIG. 4. Comparison between the composite expansion Eq. (36) and the numerical results for $\mathcal{F} = 15$. (a) The depth of liquid along the centerline of the steady flow past a cylinder as a function of the downstream distance, x , for $\mathcal{F} = 15$. The composite expansion Eq. (36) shows good agreement with our numerical simulations. (b) Contours of the absolute difference between the numerical result and the composite expansion for the flow thickness. The error does not exceed 1.1% of the upstream flow depth.

We have obtained the asymptotic approximations for the flow depth in the inner region in which r is order 1 [Eq. (33)] and the outer region in which r is order \mathcal{F} [Eq. (32)]. By adding these expressions and subtracting the common terms in the matching region, we can obtain the following composite expansion:

$$h_{\text{com}} = 1 - 3\mathcal{F}^{-2}/(4r^2) + (3/2)\mathcal{F}^{-2}\{K_0[3r/(2\mathcal{F})] - \cos\theta K_1[3r/(2\mathcal{F})]\}e^{(3r\cos\theta)/(2\mathcal{F})}, \quad (36)$$

which is an excellent approximation for all r (see Fig. 4). The composite asymptotic solution accurately captures the numerical results.

The approximations found in this section are effective (and show good agreement with the numerical results) provided that $\mathcal{F} \gtrsim 5$ (see Fig. 3).

Finally, we comment on the validity of the lubrication approximation. Close to the cylinder lubrication theory breaks down. The region in which the neglected effects of the no-slip boundary condition are important is given by $r - 1 \sim H_\infty/L \ll 1$. The inner region of our asymptotic analysis corresponds to $r \sim 1$. Thus, the region in which no-slip is important is much smaller than the inner region.

B. Force exerted on the cylinder

In many practical applications, it is important to estimate the downslope component of force exerted by the flow on the cylinder. We use our asymptotic approximations to calculate this force in the regime $\mathcal{F} \gg 1$. The force consists of a hydrostatic component arising from the pressure and a dynamic component associated with gradients in the flow velocity. The dimensional force owing to

the pressure is

$$\int_0^{2\pi} \int_0^{H(L,\theta)} -P \cos \theta L d\theta dZ, \quad (37)$$

where P is the dimensional hydrostatic pressure at the cylinder boundary, $P = \Delta \rho g H_\infty \cos \beta (h - z)$, from which we obtain

$$\int_0^{2\pi} \int_0^H -P \cos \theta L dZ d\theta = \pi \mathcal{F}^{-1} \Delta \rho g H_\infty^2 L \cos \beta = \pi \Delta \rho g H_\infty L^2 \sin \beta, \quad (38)$$

to leading order, where we have used the inner expansion Eq. (33) for the flow depth. This force corresponds to the component of the weight of the cylinder filled with fluid up to a height H_∞ acting along the slope. Calculation of the dynamic component of the force requires detailed knowledge of the flow close to the cylinder where no-slip is important, which is beyond the scope of this article.

V. FLOW PAST A WIDE CIRCULAR CYLINDER ($\mathcal{F} \ll 1$)

In this section, we analyze the regime $\mathcal{F} \ll 1$, corresponding to a steep slope relative to the ratio of the far upstream depth to the cylinder radius. Figure 2(c), a contour plot of the numerical results for $\mathcal{F} = 0.025$, illustrates that in this wide cylinder regime, dry zones in which there is no liquid occur downstream of the cylinder. Figure 2(c) also illustrates how the flow accumulates in a small but deep region upstream of the cylinder, within which the flow depth is considerably enhanced as a result of its deflection. For the case plotted in Fig. 2(c), the maximum flow depth is 3.57 when $\mathcal{F} = 0.025$. We apply asymptotic methods to interpret the structure of the flow in the deep upstream region. We introduce an inner asymptotic region close to $r = 1$, writing

$$r = 1 + \mathcal{F}^a s \quad \text{and} \quad h = \mathcal{F}^b \mathcal{H}. \quad (39)$$

We balance the leading-order terms in the governing Eq. (7); $\cos \theta \partial h^3 / \partial r \sim \mathcal{F} \partial^2 h^4 / \partial r^2$, which leads to the requirement that

$$b = a - 1. \quad (40)$$

The governing equation in the inner region can then be written in terms of s and \mathcal{H} as

$$\cos \theta \frac{\partial \mathcal{H}^3}{\partial s} - \frac{\mathcal{F}^a \sin \theta}{1 + \mathcal{F}^a s} \frac{\partial \mathcal{H}^3}{\partial \theta} = \frac{1}{4} \left[\frac{\partial^2 \mathcal{H}^4}{\partial s^2} + \frac{\mathcal{F}^a}{1 + \mathcal{F}^a s} \frac{\partial \mathcal{H}^4}{\partial s} + \frac{\mathcal{F}^{2a}}{(1 + \mathcal{F}^a s)^2} \frac{\partial^2 \mathcal{H}^4}{\partial \theta^2} \right]. \quad (41)$$

The boundary condition Eq. (10) at the edge of the cylinder ($s = 0$) is

$$\cos \theta - \frac{\partial \mathcal{H}}{\partial s} = 0 \quad \text{or} \quad \mathcal{H} = 0. \quad (42)$$

The form of Eq. (41) suggests the following expansion for \mathcal{H} :

$$\mathcal{H} = \mathcal{H}_0 + \mathcal{F}^a \mathcal{H}_1 + \dots \quad (43)$$

To leading order, we obtain

$$\cos \theta \frac{\partial \mathcal{H}_0^3}{\partial s} = \frac{1}{4} \frac{\partial^2 \mathcal{H}_0^4}{\partial s^2}. \quad (44)$$

Integrating twice and applying the boundary condition Eq. (42), we obtain the linear profile

$$\mathcal{H}_0 = s \cos \theta + G(\theta), \quad (45)$$

where $G(\theta)$ is an arbitrary function, which is to be determined. Equation (45) implies that to leading order the flow depth is horizontal, forming a pond upstream of the cylinder. Such a feature has previously been shown to develop upstream of a mound of sufficient amplitude [18] and upstream of an injection source (see Fig. 3 of Ref. [33]).

The governing Eq. (41) at $\mathcal{O}(\mathcal{F}^a)$ is

$$\cos \theta \frac{\partial}{\partial s} (3\mathcal{H}_0^2 \mathcal{H}_1) - \sin \theta \frac{\partial \mathcal{H}_0^3}{\partial \theta} = \frac{1}{4} \frac{\partial}{\partial s} (\mathcal{H}_0^4) + \frac{\partial^2}{\partial s^2} (\mathcal{H}_0^3 \mathcal{H}_1), \quad (46)$$

with boundary condition $\partial \mathcal{H}_1 / \partial s = 0$ at $s = 0$. The solution, in terms of \mathcal{H}_0 , is

$$\mathcal{H}_1 = k_{-2}(\theta) \mathcal{H}_0^{-2} + k_0(\theta) + k_1(\theta) \mathcal{H}_0 + k_2(\theta) \mathcal{H}_0^2, \quad (47)$$

where $k_0(\theta)$ is an arbitrary function arising from integration and

$$k_{-2}(\theta) = -\frac{1}{8 \cos \theta} \frac{d}{d\theta} (G^4 \tan \theta), \quad k_1(\theta) = -\frac{G \tan^2 \theta + G' \tan \theta}{\cos \theta}, \quad k_2(\theta) = \frac{3 \tan^2 \theta - 1}{8 \cos \theta}. \quad (48)$$

When \mathcal{H}_0 vanishes, the series becomes nonasymptotic. We denote this location as

$$s = s_*(\theta) = \frac{-G(\theta)}{\cos \theta}. \quad (49)$$

Also, the leading-order behavior for the depth Eq. (45) does not satisfy the boundary condition $h \rightarrow 1$ as $r \rightarrow \infty$. Hence, near s_* , we must introduce an interior region to match the inner expansion to a far-field expansion in which $h \rightarrow 1$. To capture the behavior in this region, we write

$$s = s_* + \mathcal{F}^c \eta, \quad (50)$$

where c is another exponent to be determined. The behavior of the leading-order function near the interior region is $\mathcal{H}_0 = \mathcal{F}^c \eta \cos \theta$ and for $|s - s_*| \ll 1$,

$$\mathcal{H}_1 \sim k_{-2}(\theta) \mathcal{H}_0^{-2} = \frac{k_{-2}(\theta)}{\mathcal{F}^{2c} \eta^2 \cos^2 \theta}. \quad (51)$$

In the interior region, the first two terms in the expansion for the depth are

$$h = \mathcal{F}^b \mathcal{H}_0 + \mathcal{F}^{b+a} \mathcal{H}_1 = \mathcal{F}^{b+c} \eta \cos \theta + \mathcal{F}^{b+a-2c} k_{-2}(\theta) / (\eta \cos \theta)^2 + \dots \quad (52)$$

and this must be the behavior as $\eta \rightarrow -\infty$. Conversely, as $\eta \rightarrow \infty$, we must find that $h \rightarrow 1$. Thus, we can determine that $b + c = 0$ and $b + a - 2c = 0$. By combining these conditions with Eq. (40), we obtain the exponents

$$a = 3/4, \quad b = -1/4, \quad c = 1/4. \quad (53)$$

We match the inner solution to the upstream flow depth ($h = 1$) through the interior region to obtain the function of integration (for details, see Appendix B),

$$G(\theta) = (-4 \cos \theta)^{1/4}, \quad (54)$$

for $\pi/2 < \theta < 3\pi/2$. Note that $G(\pi) = \sqrt{2}$ and $G(\pi/2) = 0$. Upstream of the cylinder, near $r = 1$, the depth to leading order varies linearly with radial distance, given by

$$h = \mathcal{F}^{-1/4} \mathcal{H}_0 = 2^{1/2} \mathcal{F}^{-1/4} (-\cos \theta)^{1/4} + \mathcal{F}^{-1} \cos \theta (r - 1), \quad (55)$$

which we compare to the numerical results along the line of symmetry (the $x < 0$ axis along which $\theta = \pi$) in Fig. 5. We also plot the interior approximation, given by the solution to Eq. (B5), as a red dot-dashed line. The asymptotic approximations accurately capture the behavior.

To leading order, we determine from Eq. (55) that the free surface is horizontal in a region of lengthscale $\mathcal{F}^{3/4}$ upstream of the cylinder and there is a pond of nearly stationary liquid there. Correspondingly, the radial velocity Eq. (8) is zero to leading order in this region, while the azimuthal velocity is Eq. (9),

$$u_\theta = \frac{3}{2} z (2h - z) [-r^{-1} \sin \theta + \mathcal{O}(\mathcal{F}^{3/4})]. \quad (56)$$

The leading-order expression for the depth Eq. (55) may also be obtained by balancing volume fluxes in the pond region. This method has previously been employed to calculate the flow depth

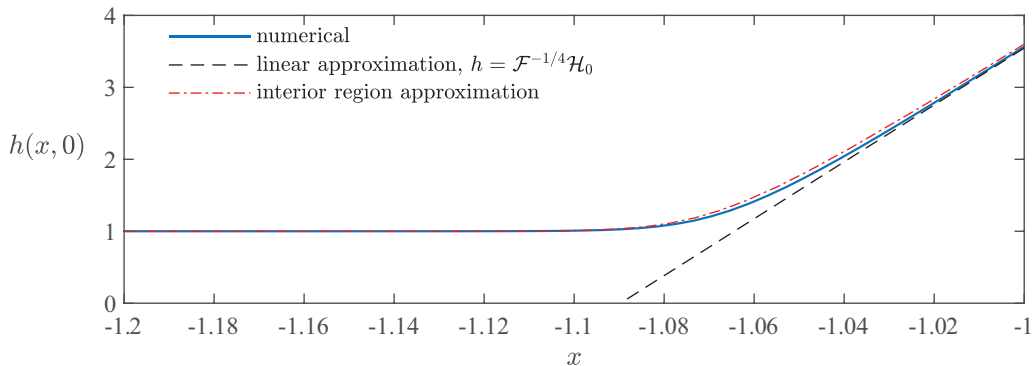


FIG. 5. Depth along the centerline for the steady flow past a cylinder as a function of distance, x , with $\mathcal{F} = 0.025$. The depth from our numerical simulations (solid blue line) is compared to the “inner” approximation [black dashed line, Eq. (55)], which varies linearly with x , and is very close to the “interior” approximation (red dot-dashed line), the solution to Eq. (B2), which is plotted in Fig. 18.

upstream of a squeegee moving horizontally over a layer of viscous fluid, which is governed by a similar but not identical lubrication model (see Lister [55]).

The flow depth in the pond region upstream of the cylinder, which has a horizontal free surface, is given by $h_p = \mathcal{F}^{-1} \cos \theta (r - 1) + \hat{G}(\theta)$, where $\hat{G}(\theta)$ is to be determined (this is the equivalent of (45)). The pond extends to $r = 1 - \mathcal{F} \hat{G}(\theta) / \cos \theta$, where the flow depth returns to order unity [this is the equivalent of Eq. (49)]. The flux into the pond from upstream between $\theta = \pi$ and $\theta = \theta_0$ is $\sin \theta_0$ as the upstream flow depth is unity. The flux out of the segment of the pond in $\theta_0 < \theta < \pi$ occurs across $\theta = \theta_0$ and balancing the fluxes in and out of this region yields

$$\sin \theta_0 = \int_{r=1}^{r=1 - \mathcal{F} \hat{G}(\theta_0) / \cos \theta_0} h_p^3 \left(\sin \theta_0 + \frac{\mathcal{F}}{r} \frac{\partial h_p}{\partial \theta} \right) dr. \quad (57)$$

Upon substituting for h_p and integrating, we obtain $\hat{G}(\theta) = \mathcal{F}^{-1/4} (-4 \cos \theta)^{1/4}$ to leading order, which is identical to $G(\theta)$ derived using the more complete asymptotic techniques. The volume flux method avoids the need for explicitly constructing the interior layer Eq. (50), instead establishing the leading-order behavior by matching conditions. It is more direct than the formal matched asymptotic expansions, but does not easily extend to higher orders. Nevertheless, we use it to analyze the flow around square and wedge-shaped cylinders (Secs. VII and VIII) in the regime $\mathcal{F} \ll 1$, noting that these results are identical to the leading results from matched asymptotic expansions.

On the boundary of the cylinder ($r = 1$) we find that the flow thickness is

$$h = \mathcal{F}^{-1/4} (-4 \cos \theta)^{1/4}, \quad (58)$$

which is compared to the numerical results in Fig. 6. We note that there is very good agreement between the numerical and asymptotic result close to the upstream stagnation point ($\theta = \pi$), but as the edge of the cylinder is approached ($\theta = \pi/2$), the agreement declines, indicating that a different asymptotic balance arises in that zone.

The maximum flow thickness is attained at the upstream stagnation point, $(r, \theta) = (1, \pi)$, and is given by

$$h_{\max} = \mathcal{F}^{-1/4} 2^{1/2}. \quad (59)$$

This leading-order prediction for the maximum flow thickness shows good agreement with the numerical results when $\mathcal{F} \ll 1$ (see Fig. 7).

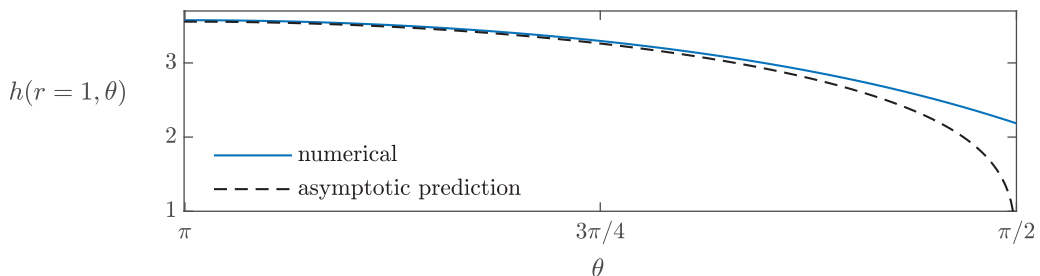


FIG. 6. Flow thickness on the upstream cylinder boundary, $h(1, \theta)$, as a function of polar angle θ for $\mathcal{F} = 0.025$. The numerically calculated flow thickness (solid curve) is compared to the asymptotic approximation, $h(1, \theta) = \mathcal{F}^{-1/4}G(\theta)$, Eq. (58) (dashed curve).

To obtain the second-order term in the maximum flow depth,

$$h_{\max} = \mathcal{F}^{-1/4}\mathcal{H}_0(s=0, \theta=\pi) + \mathcal{F}^{1/2}\mathcal{H}_1(s=0, \theta=\pi) + \dots \quad (60)$$

requires determining $k_0(\pi)$ [see Eq. (47)]. This is achieved by matching at higher order in the interior region and we provide details in Appendix C. We obtain $k_0(\pi) = -17/40$ and the improved approximation for the maximum flow depth is

$$h_{\max} = 2^{1/2}\mathcal{F}^{-1/4} + (3/40)\mathcal{F}^{1/2} + \dots, \quad (61)$$

which shows good agreement with the numerical results (blue dashed line in Fig. 7).

In Fig. 8, we compare this improved approximation with the numerical results and include the asymptotic predictions for the maximum flow depth from Sec. IV (for $\mathcal{F} \gg 1$). The empirical expression

$$h_{\max} = (1 + 4\mathcal{F}^{-1})^{1/4} \quad (62)$$

agrees with the small \mathcal{F} expansion Eq. (61) to leading order in the regime $\mathcal{F} \ll 1$ and agrees with the large \mathcal{F} expansion Eq. (34) to order \mathcal{F}^{-1} in the regime $\mathcal{F} \gg 1$. Indeed, the simple expression Eq. (62) quite accurately captures the behavior of the maximum flow depth for all \mathcal{F} (see Fig. 8). The error between Eq. (62) and the numerical results for the maximum depth never exceeds 3.5%.

Finally, we comment on the validity of the lubrication approximation close to the cylinder. The region in which the neglected effects of the no-slip boundary condition are important is given by

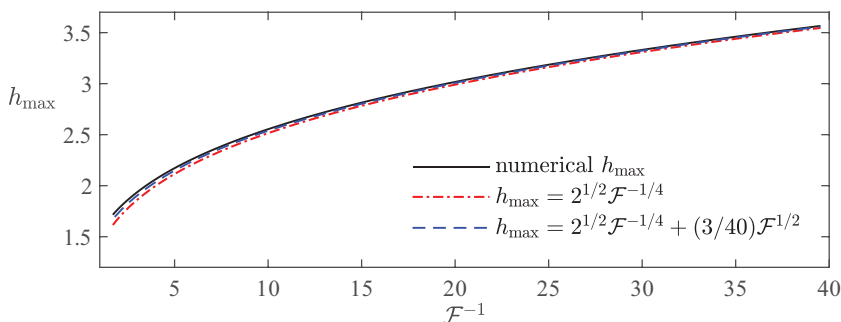


FIG. 7. The maximum depth, for steady flow past a cylinder as a function of \mathcal{F}^{-1} . The deepest point is always at the stagnation point on the upstream boundary at $\theta = \pi$. The results from our numerical technique (solid black line) compare very closely to the leading-order prediction of Eq. (58) (red dot-dashed line) and there is particularly good agreement for $\mathcal{F} \ll 1$. The asymptotic expansion with the second term Eq. (61) is also plotted (blue dashed line).

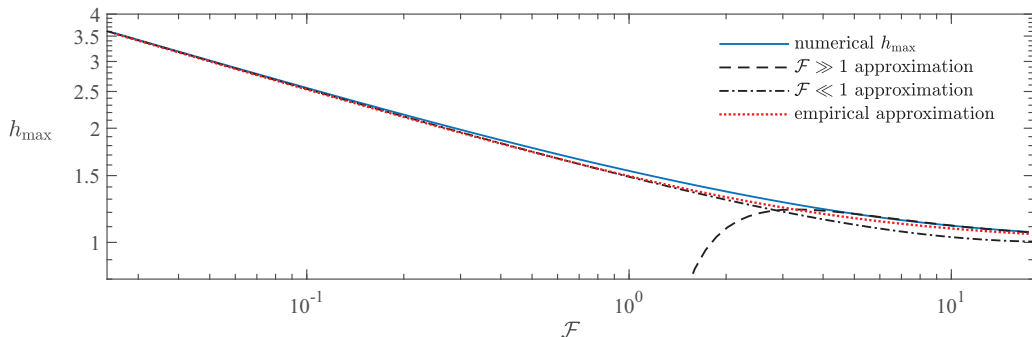


FIG. 8. The maximum thickness for steady flow past a cylinder as a function of \mathcal{F} . The numerical results are compared to our asymptotic predictions for the two regimes; $\mathcal{F} \ll 1$ [Eq. (61)] and $\mathcal{F} \gg 1$ [Eq. (34)]. We also include our empirical approximation Eq. (62) as a dotted red line.

$r - 1 \sim H_\infty/L \ll 1$. The pond region is $r - 1 \sim \mathcal{F}^{3/4}$. Therefore, the region in which no-slip is important is much smaller than the pond region provided that $\tan \beta \ll \mathcal{F}^{-1/4}$, which holds in the present regime, $\mathcal{F} \ll 1$.

A. Force exerted on the cylinder

The dimensional force on the cylinder owing to the pressure is given by Eq. (37). In the regime $\mathcal{F} \ll 1$, the dominant contribution to this force arises from the upstream pond and so we calculate the integral of the pressure only on the upstream boundary ($\pi/2 < \theta < 3\pi/2$). By considering symmetry about the centerline, we find the dimensional force exerted on the cylinder due to pressure to be

$$2L \int_{\pi/2}^{\pi} \int_0^H -P \cos \theta dZ d\theta = \mathcal{F}^{-1/2} \Delta \rho g H_\infty^2 L \cos \beta \int_{\pi/2}^{\pi} G(\theta)^2 \cos \theta \quad (63)$$

$$= 1.865 \mathcal{F}^{-1/2} \Delta \rho g H_\infty^2 L \cos \beta. \quad (64)$$

VI. LABORATORY EXPERIMENTS

We carried out a series of laboratory experiments on an inclined slope of width 30cm and length 120cm in the downslope direction [see Fig. 9(a)]. Golden syrup was released from a lock gate behind which a fixed depth of syrup was maintained by hand to provide a constant head. The downslope flow from a constant-flux line source evolved into a steady current with constant thickness, H_∞ .

A cylinder was held fixed in the center of the slope and we measured the flow thickness, H_∞ , far upstream of the cylinder. After a sufficient time, the flow past the cylinder became steady. We observed that the far upstream, constant thickness flow is perturbed in a neighbourhood of the cylinder. The flow deepened upstream and became shallower downstream of the cylinder [see Fig. 9(b)].

The minimum and maximum thicknesses of the steady flow occur at the edge of the cylinder, at the most downstream and most upstream points, respectively. We performed a series of experiments in which we varied the inclination of the plane, the radius of the cylinder and the source flux per unit width. We measured the far upstream, minimum and maximum thicknesses using a laser line following a technique that has previously been used for measuring the thickness of a free surface [56,57] and a deformed elastic sheet [58,59].

A laser line was directed onto black paper laid on the tank base and photographed. The image could then be compared to later images of the laser shining onto syrup flowing down the tank to determine the flow thickness. The laser is directed to illuminate the centerline of the tank. This

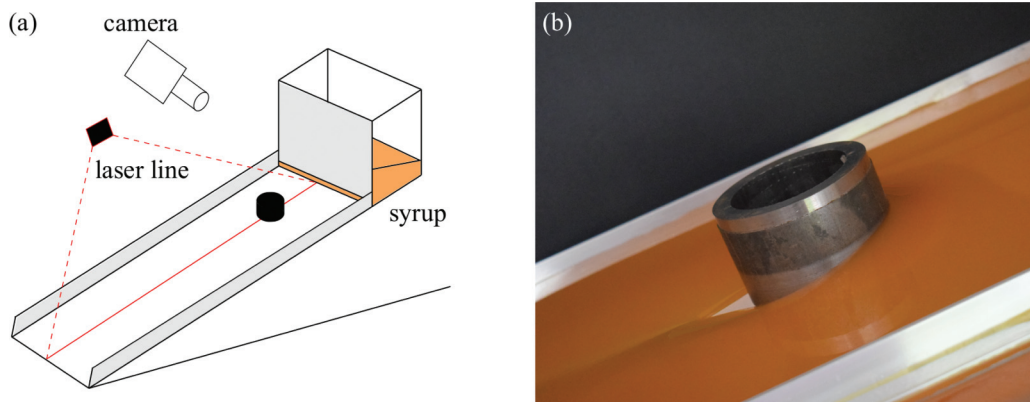


FIG. 9. (a) Schematic of the experimental setup. A constantly maintained head of syrup supplies constant flux. (b) Photograph of the steady syrup flow past the cylinder, illustrating the increase in flow depth upstream of the cylinder, the sharp decrease in flow depth around the cylinder and the dry region downstream.

technique required the syrup to be opaque, which was achieved by adding a few drops of magnolia paint to the syrup. The mixture was tested in a rheometer to confirm that it was still Newtonian, with viscosity 89.6 Pa s. We note that the results presented below for the dimensionless flow depth, $h = H/H_\infty$, do not require knowledge of the viscosity of the fluid. We require only the flow depth $H(X, Y)$ and the far upstream flow depth H_∞ (which is dependent on the viscosity) to be measured, as well as the slope angle and cylinder radius. Thus, although changes in the laboratory temperature from experiment to experiment can have a strong effect on the viscosity of the syrup, they do not lead to errors in the experimental data for the dimensionless flow depth.

A. Results

Our results are shown in Table I. The minimum and maximum flow thicknesses are compared to our numerical results in Fig. 10, which show very good agreement. The flow thickness of the syrup

TABLE I. Experimental results of the minimum and maximum flow thicknesses.

Angle (degrees)	Cylinder radius R (mm)	Flow thickness H_∞ (mm)	Parameter \mathcal{F}	Experimental max. h_{\max} (dimensionless)	Experimental min. h_{\min} (dimensionless)
5.0	24	15	7.14	1.2	0.85
3.5	48	13.2	4.50	1.72	0.61
5.0	24	7.9	3.76	1.28	0.77
3.5	48	9.8	3.34	1.22	0.57
10.0	24	7.4	1.75	1.38	0.53
14.6	24	8.5	1.36	1.63	0.43
13.0	24	5.5	0.99	1.7	0
14.6	24	6	0.96	1.71	0.38
15.0	24	6	0.93	1.56	0.32
10.0	40.5	6.5	0.91	1.61	0
20.0	24	7.9	0.90	1.64	0
20.0	40.5	11	0.75	1.68	0
23.1	40.5	12.1	0.70	1.64	0
23.1	40.5	8	0.47	1.76	0

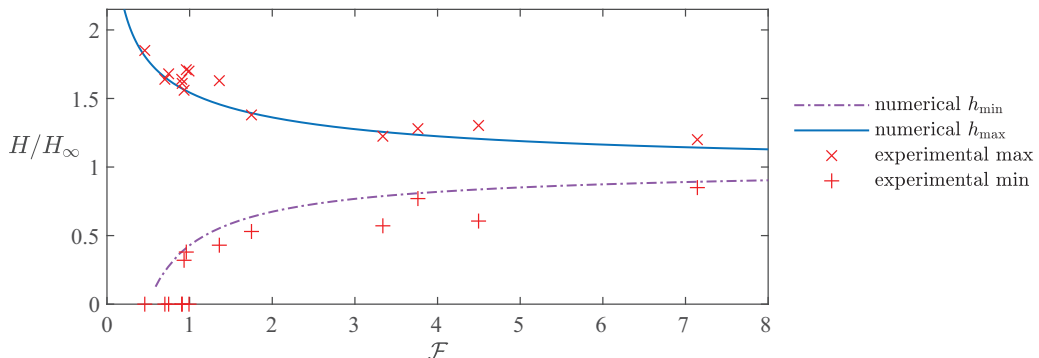


FIG. 10. Comparison of the experimental and theoretical results (calculated numerically) for the maximum and minimum flow thicknesses. Zero minimum flow thickness corresponds to a dry zone downstream of the cylinder in which there is no syrup.

along the centerline upstream of the cylinder determined using the laser line technique is compared to our numerical results in Fig. 11 for three values of \mathcal{F} .

In general, the experiments showed a slightly larger increase in flow thickness upstream of the cylinder compared to the theory. This may be because the theory neglects the no-slip condition at the cylinder wall, which will slow the flow here and lead to an increased build-up of liquid upstream.

The small discrepancy could also be caused by surface tension, which was neglected in the model (see Sec. II). At room temperature, the density of the syrup is 1400 kg m^{-3} and we take its surface tension coefficient to be $\sigma = 0.08 \text{ N m}^{-1}$ [60]. With these values, the capillary length and Bond number are

$$l_c = \sqrt{\frac{\sigma}{\Delta\rho g}} = 2.4 \text{ mm}, \quad \text{Bo} = \frac{\Delta\rho g L^2}{\sigma} = 280, \quad (65)$$

where we have used a streamwise lengthscale $L = 40 \text{ mm}$, which is the radius of the larger cylinder used in the experiments. These values suggest that the influence of surface tension is negligible upstream of the cylinder, except perhaps in a region very close to the cylinder and the contact line if a dry region forms. The depth-averaged velocity of the fluid was typically

$$U = \frac{\Delta\rho g H_\infty^2 \sin\beta}{3\mu} \approx 1 \text{ mm s}^{-1}. \quad (66)$$

The Reynolds number is then

$$\text{Re} = \frac{\rho U L}{\mu} = 6 \times 10^{-4}, \quad (67)$$

which is very small, confirming that inertia is negligible in the experiments.

The numerical results predict that a dry region in which $h = 0$ occurs downstream of the cylinder only when $\mathcal{F} < 0.47$. However, the experimental results often have a dry region for values of \mathcal{F} larger than this (i.e., $h_{\min} = 0$; see Fig. 10). This discrepancy is most likely due to contact angle effects at the edge of the dry region. The associated force resists the spreading of the thin syrup film and this is not accounted for in the model. The difference may also be due to the no-slip condition being neglected, which resists syrup flowing around the downstream side of the cylinder. Alternatively, it may be a result of very slow temporal convergence to the steady state downstream of the cylinder and that the experimental runs had not fully attained their steady-state.

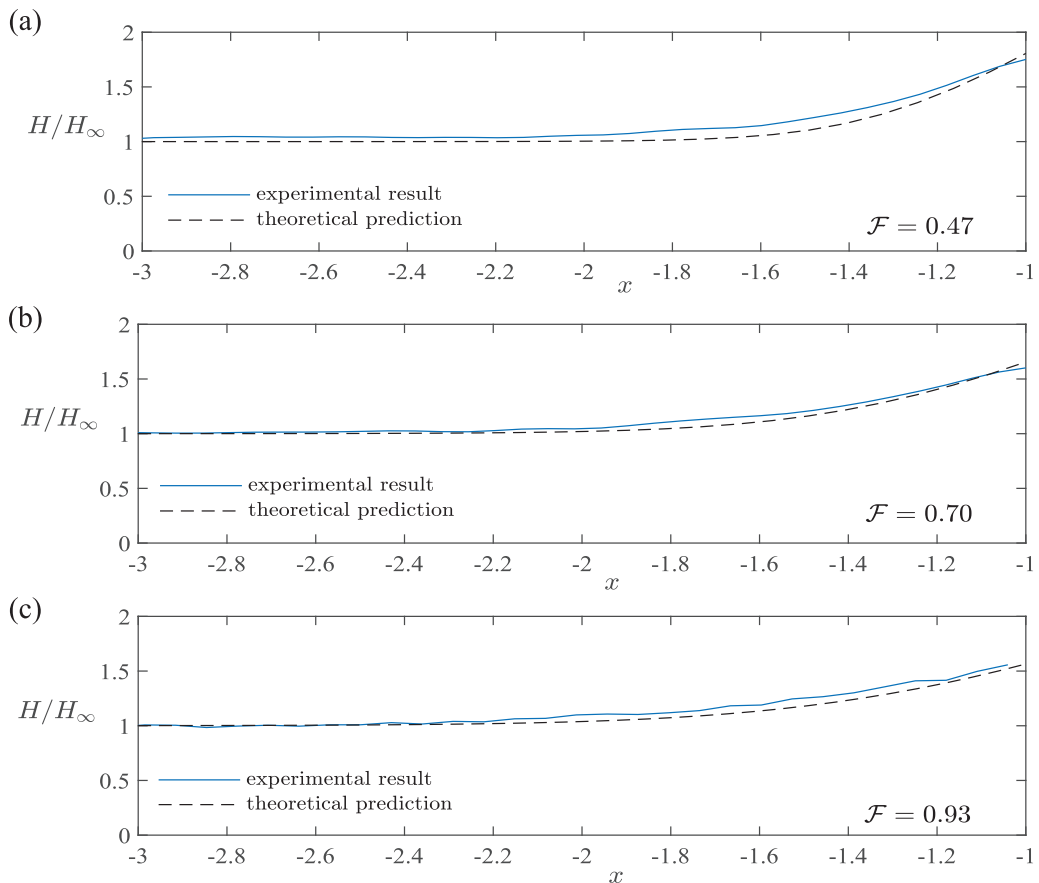


FIG. 11. Flow depth along the centerline as a function of dimensionless distance, x , upstream of the cylinder for three values of the flow parameter, \mathcal{F} . The experimental results (solid line) obtained from the laser line technique show very good agreement with our theoretical predictions (dashed lines), calculated using the numerical scheme described in Sec. III.

VII. FLOW PAST SQUARE CYLINDERS

In this section, we analyze steady free-surface viscous flow past a square cylinder, of side length $2L$. The dimensionless governing equation is given by Eq. (4), while boundary conditions enforce $\mathbf{u} \cdot \mathbf{n} = 0$ on the surface of the square and $h \rightarrow 1$ as $|\mathbf{x}| \rightarrow \infty$. The square is centered on the origin and its upstream boundary is at $x = -1$ (see Fig. 12). We adapt our numerical technique for this geometry and in the case that there are dry regions downstream of the square, we add a small source on the downstream boundary at $x = 1$ (see Sec. III). Contour plots of the numerical results for $\mathcal{F} = 10$ and $\mathcal{F} = 0.25$ are shown in Fig. 12. In the regime $\mathcal{F} \gg 1$, there is a small perturbation to the flow depth [Fig. 12(a)] and the behavior is broadly similar to that for flow past a circular cylinder in the same regime. In particular the perturbation to the flow depth is approximately antisymmetric in $x = 0$. The behavior in the regime of a relatively wide square cylinder ($\mathcal{F} \ll 1$) is however significantly different from the wide circular cylinders analyzed in Sec. V. Henceforth, in the present section, we restrict our attention to the regime $\mathcal{F} \ll 1$.

In Sec. V, we quantified the increase in flow depth upstream of a relatively wide circular cylinder ($\mathcal{F} \ll 1$) using asymptotic analysis. We found a ponded region in which the flow depth is horizontal. In the present section, we determine the leading-order expressions for the depth and shape of the

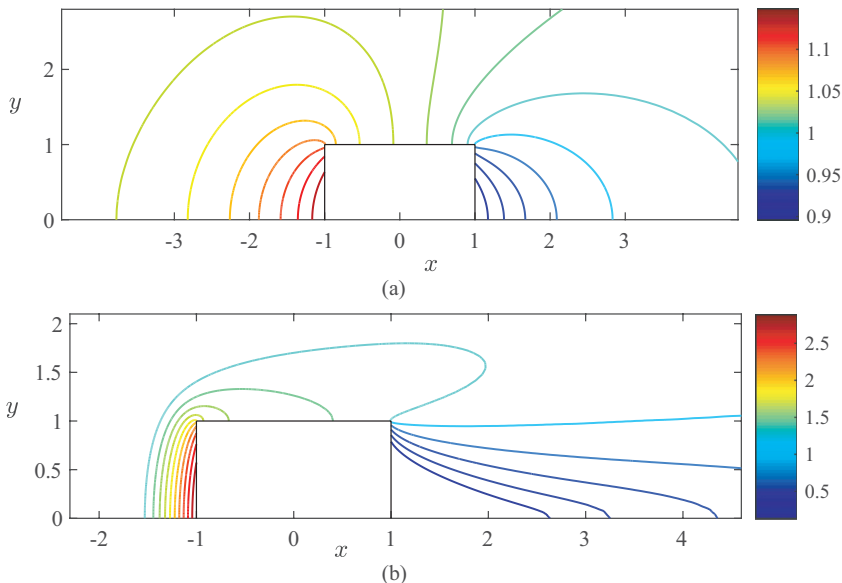


FIG. 12. Flow past a square with (a) $\mathcal{F} = 10$ and (b) $\mathcal{F} = 0.25$. The two panels have different axes to capture the region of interest. Note that the flow remains attached to the square in both cases and there is no dry region for these values of \mathcal{F} .

ponded region upstream of a square cylinder by balancing the volume flux in the pond rather than repeating the asymptotic analysis of Sec. V, although such an expansion with “inner,” “interior,” and “outer” regions may be constructed and is necessary to extend the results beyond their leading-order form. Importantly, we find that the depth within the pond upstream of a square cylinder has a different scaling in its dependence on \mathcal{F} from the case of a circular cylinder.

The no-flux condition at the upstream boundary is

$$1 - \mathcal{F} \frac{\partial h}{\partial x} = 0 \quad \text{at } x = -1, \quad \text{provided } h > 0. \quad (68)$$

We also require that the flow depth returns to its unperturbed value far from the square,

$$h \rightarrow 1 \quad \text{as } x \rightarrow -\infty. \quad (69)$$

The liquid within the ponded region just upstream of the square has the following depth [cf. Eq. (45)]:

$$h_p = \mathcal{F}^{-1}(1 + x) + G_s(y), \quad (70)$$

where the prefactor, \mathcal{F}^{-1} is chosen to satisfy the boundary condition at $x = -1$ Eq. (68) and $G_s(y)$ represents the flow depth on $x = -1$ and is to be determined. The edge of the pond, where the flow depth returns to order unity, is given by the solution to $h_p = 0$, which is

$$x_u(y) = -1 - \mathcal{F}G_s(y). \quad (71)$$

The flux into the pond from upstream, between $y = 0$ and $y = \mathcal{Y}$, is simply \mathcal{Y} . The flux out of this region of the pond is the integral of the cross-slope flux from $x = x_u(\mathcal{Y})$ to $x = -1$ at $y = \mathcal{Y}$ (since there is no flux across $y = 0$). In steady state, we balance these fluxes, which yields

$$\mathcal{Y} = \int_{x=x_u(\mathcal{Y})}^{x=-1} -\mathcal{F}h_p^3 \frac{\partial h_p}{\partial y} dx. \quad (72)$$

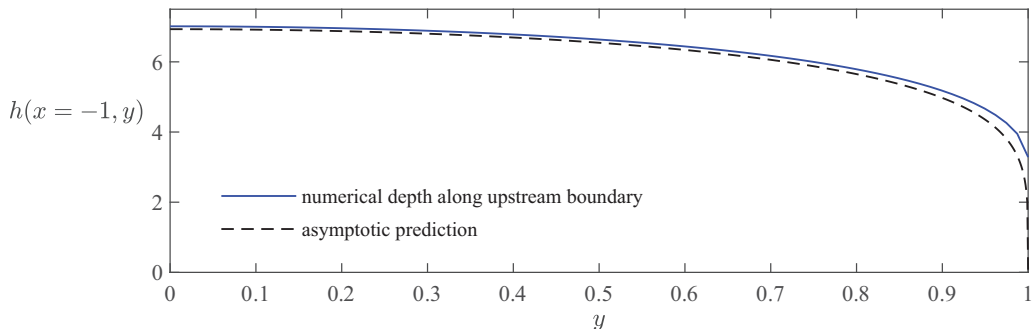


FIG. 13. Flow depth as a function of position along the upstream boundary of the rectangle for $\mathcal{F} = 0.025$. The asymptotic prediction is $h = \mathcal{F}^{-2/5}G(y)$ where the function $G(y)$ is given by Eq. (74).

Then using $G'_s(0) = 0$, owing to symmetry, we obtain

$$G_s(y) = 10^{1/5}\mathcal{F}^{-2/5}(a_0 - y^2)^{1/5}, \quad (73)$$

where a_0 is a constant of integration. Near the cross-stream edge of the square (at $y = 1, x = -1$), the pond ends and the flow depth is no longer of order $\mathcal{F}^{-2/5}$. Thus, we find $a_0 = 1$. The flow depth along the upstream wall at $x = -1$ is

$$h = \mathcal{F}^{-2/5}10^{1/5}(1 - y^2)^{1/5}. \quad (74)$$

Along the upstream wall, the numerically calculated flow thickness is compared to this asymptotic prediction Eq. (74) in Fig. 13. The asymptotic scaling for the flow depth in the pond is $h \sim \mathcal{F}^{-2/5}$ and the extent of the pond upstream is $x_u \sim \mathcal{F}^{3/5}$. Notably these are different from the circular cylinder [cf. Eq. (53)].

The maximum depth occurs at $y = 0, x = -1$ and is

$$h_{\max} = 10^{1/5}\mathcal{F}^{-2/5}, \quad (75)$$

which shows good agreement with numerical results for small \mathcal{F} (see Fig. 14).

The increase in flow depth upstream of the square Eq. (75) has a different scaling to that for a circular cylinder Eq. (59). The flow depth increases more significantly for a square because the

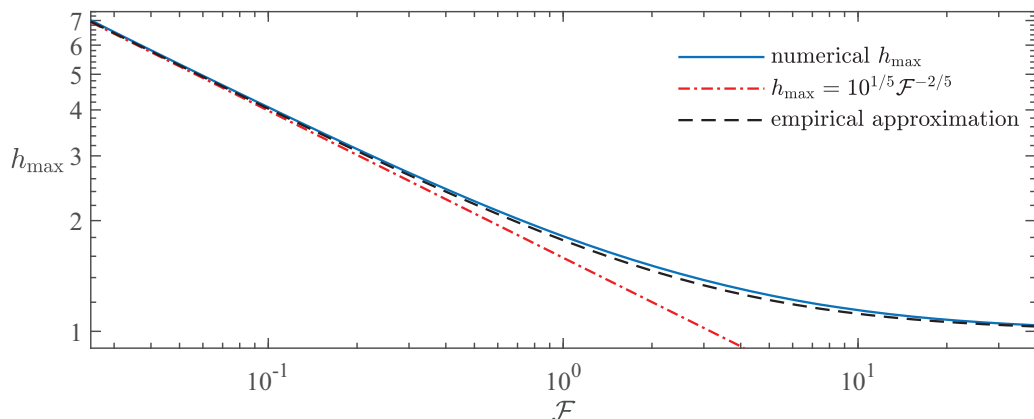


FIG. 14. Maximum thickness for flow past a square cylinder as a function of the dimensionless flow parameter, \mathcal{F} . The asymptotic prediction is $h_{\max} = 10^{1/5}\mathcal{F}^{-2/5}$, Eq. (75) and is accurate for $\mathcal{F} \ll 1$. The empirical approximation is quite accurate for all \mathcal{F} and is given by Eq. (76).

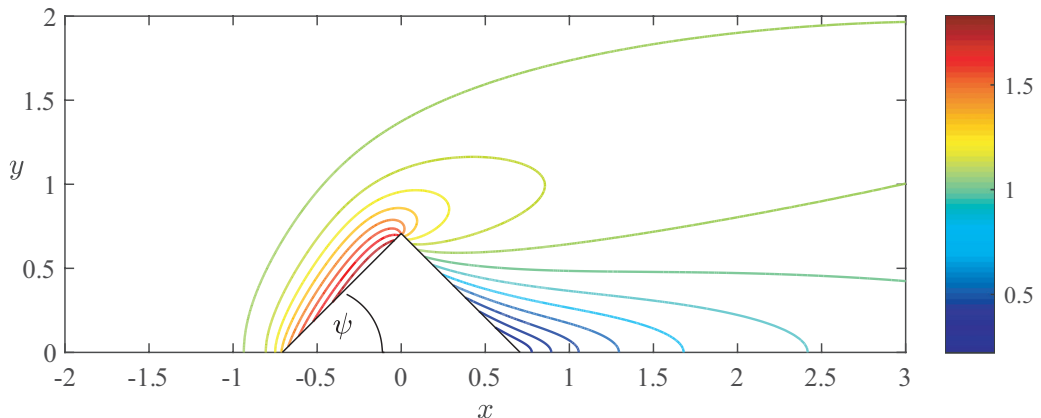


FIG. 15. Flow past a rhombus with $\mathcal{F} = 0.25$. The angle between the upstream boundary and the centerline is $\psi = \pi/4$. The rhombus sides have dimensionless length of unity. There is no dry region for $\mathcal{F} = 0.25$.

curvature at the upstream boundary of the square is zero whereas the curvature of a circle is finite. In the next section, we consider how the flow depth increases upstream of a wedge, which has infinite curvature at its upstream vertex.

For a circular cylinder, we obtained an empirical approximation Eq. (62) for the maximum flow depth, which was accurate for all \mathcal{F} . For a square cylinder, the expression

$$h_{\max} = (1 + 10^{1/2} \mathcal{F}^{-1})^{2/5} \quad (76)$$

agrees to leading order with the small \mathcal{F} approximation (75) in the regime $\mathcal{F} \ll 1$. Although we have not established the expansion for the depth in the regime $\mathcal{F} \gg 1$, Eq. (76) provides an excellent approximation to the numerical results for all \mathcal{F} as shown in Fig. 14. The error between the approximation Eq. (76) and the numerical results never exceeds 3.5%.

The results in this section pertain to the flow depth upstream of a square but the analysis is independent of the streamwise length of the square. Thus, the results apply more generally to rectangular cylinders.

Finally, we calculate the force exerted on a square cylinder. We assume that the dominant contribution is from the weight of the liquid in the pond (as was the case for a circular cylinder, see Sec. V A). The force exerted is

$$2 \int_0^L \int_0^H P dZ dY = 2.05 \mathcal{F}^{-4/5} \Delta \rho g H_\infty^2 L \cos \beta, \quad (77)$$

which is higher order with respect to \mathcal{F} than the force exerted on a circular cylinder Eq. (63).

VIII. FLOW PAST A RELATIVELY WIDE WEDGE ($\mathcal{F} \ll 1$)

In this section, we consider steady free-surface viscous flow past a cylinder with rhombus cross section. Each side of the rhombus has length L . The dimensionless setup is shown in Fig. 15; the rhombus is centered at the origin and the angle between the upstream boundary and the centerline is denoted by ψ .

The dimensionless governing equation is as before Eq. (4). We adapt our numerical technique for this geometry and in the case that there are dry regions, we add a small source on the downstream boundary of the rhombus (see Sec. III). A contour plot of the numerical result for $\mathcal{F} = 0.25$ is shown in Fig. 15. We note that when $\mathcal{F} \ll 1$, the flow forms a relatively deep pond on the upstream boundary of the rhombus. However, unlike the previous cases, the maximum depth is not located at

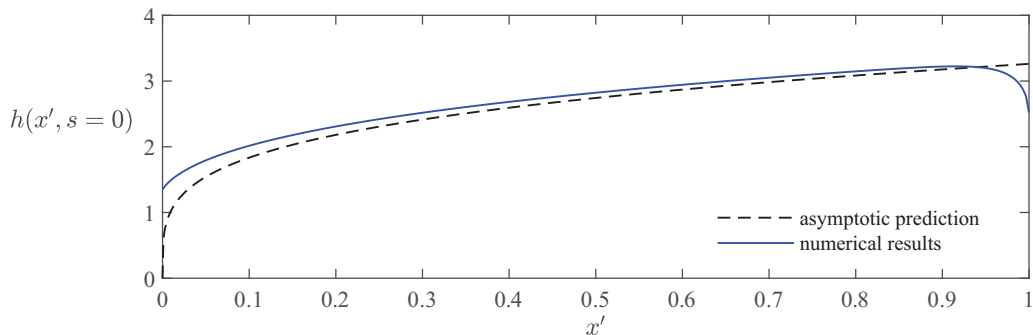


FIG. 16. Flow depth along the upstream wall for $\mathcal{F} = 0.025$ and $\psi = \pi/4$. The agreement between the numerical results and asymptotic prediction declines near $x' = 1$ as discussed in the text.

the furthest upstream position on the symmetric axis. Instead as shown in Figs. 15 and 16, the fluid depth increases with distance from the apex along the upstream boundary.

As in the previous section for flow past a square, we balance the flux in the pond region to quantify the increase in flow depth upstream of a relatively wide obstruction, $\mathcal{F} \ll 1$. We do not consider the regime of flow past a relatively narrow rhombus ($\mathcal{F} \gg 1$) as it leads to a small perturbation in the flow depth and this was studied for a circular cylinder in Sec. IV.

We begin by rotating the coordinates

$$x' = (x + \cos \psi) \cos \psi + y \sin \psi, \quad y' = -x \sin \psi + y \cos \psi.$$

In the new coordinates, the upstream wall lies along $0 < x' < 1$, $y' = \cos \psi \sin \psi$ and the governing equation becomes

$$\cos \psi \frac{\partial h^3}{\partial x'} - \sin \psi \frac{\partial h^3}{\partial y'} = \mathcal{F} \left[\frac{\partial}{\partial x'} \left(h^3 \frac{\partial h}{\partial x'} \right) + \frac{\partial}{\partial y'} \left(h^3 \frac{\partial h}{\partial y'} \right) \right]. \quad (78)$$

The no-flux condition on the upstream wall is

$$\mathcal{F} \frac{\partial h}{\partial y'} + \sin \psi = 0 \quad \text{at} \quad y' = \cos \psi \sin \psi, \quad \text{provided } h > 0. \quad (79)$$

We also require that the flow depth returns to its unperturbed value far from the obstacle,

$$h \rightarrow 1 \quad \text{as} \quad y' \rightarrow \infty. \quad (80)$$

There is a pond region near the upstream boundaries of the obstacle in which the depth is given by [cf. Eq. (70)],

$$h_p = -\mathcal{F}^{-1} \sin \psi (y' - \cos \psi \sin \psi) + G_w(x'), \quad (81)$$

where the prefactor, \mathcal{F}^{-1} is chosen to satisfy the boundary condition at $y' = \cos \psi \sin \psi$ and $G_w(x')$ represents the flow depth on the wall and is to be determined. The flux into the pond from upstream, between $x' = 0$ and $x' = \mathcal{X}$, is simply $\mathcal{X} \sin \psi$. The flux out of this region of the pond is the integral of the flux in the x' direction, which is $h_p^3 \cos \psi$ to leading order, where the component associated with the diffusive slumping is neglected as it is lower order. In steady state, we balance these fluxes as in Sec. VII to obtain the function

$$G_w(x') = \mathcal{F}^{-1/4} \left(\frac{4x' \sin^2 \psi}{\cos \psi} \right)^{1/4}. \quad (82)$$

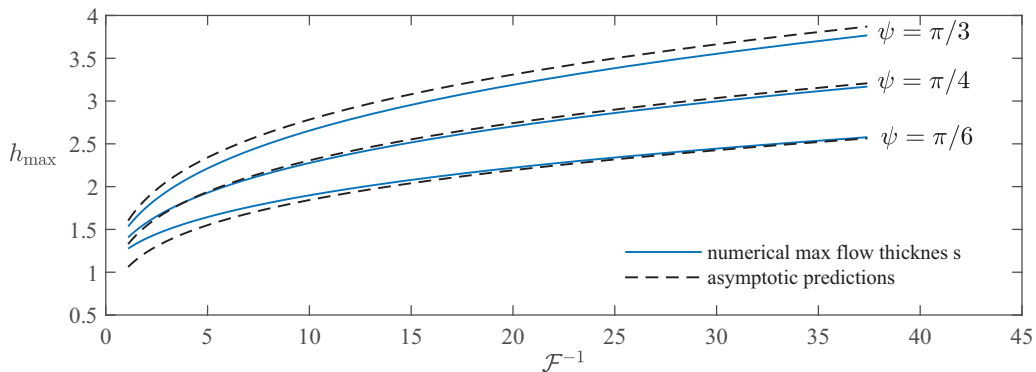


FIG. 17. Maximum flow depth as a function of the flow parameter, \mathcal{F} , for three wedge angles. The asymptotic prediction is given in Eq. (83).

The extent of the pond is order $\mathcal{F}^{3/4}$. Interestingly these scalings are identical to those found for a circular cylinder Eq. (53), but differ from the square cylinder. The difference is discussed further in the next section.

Along the wedge ($y' = \cos \psi \sin \psi$) we compare the numerically calculated flow thickness to the asymptotic result in Fig. 16 for $\psi = \pi/4$ and $\mathcal{F} = 0.025$. The agreement is good away from the edges of the wedge wall ($x' = 0$ and $x' = 1$). The asymptotic approximation is relatively poor near $x' = 1$ because it does not account for the diffusive slumping of liquid past this vertex. The size of this error increases with the angle ψ because more liquid accumulates near $x' = 1$.

From Eqs. (81) and (82), the maximum depth is at the end of the wedge, $x' = 1$, $y' = \cos \psi \sin \psi$ and is given by

$$h_{\max} = \left(\frac{4 \sin^2 \psi}{\cos \psi} \right)^{1/4} \mathcal{F}^{-1/4}. \quad (83)$$

This shows good agreement with numerical results for small \mathcal{F} and small ψ (see Fig. 17). The asymptotic approximation for the maximum thickness is not as good for blunter wedges (larger ψ) because the maximum thickness occurs further from $x' = 1$ owing to the importance of the diffusive slumping and advective terms at $x' = 1$ discussed earlier (see Fig. 16). Also, in the limit $\psi \rightarrow \pi/2$, the upstream wall is perpendicular to the oncoming flow and the flow depth scaling changes to $h \sim \mathcal{F}^{-2/5}$ (see Sec. VII).

It is straightforward to repeat the calculation for the force exerted by the hydrostatic pressure on the obstruction from the previous cases of flow past wide circular and square cylinders [Eqs. (63) and (77)]. We obtain the force to be

$$(4/3) \frac{\sin \psi}{(\cos \psi)^{1/2}} \mathcal{F}^{-1/2} \Delta \rho g H_{\infty}^2 L \cos \beta. \quad (84)$$

IX. DISCUSSION AND CONCLUSION

We have studied the deflection of a steady free-surface viscous flow on an inclined plane by a cylinder oriented perpendicular to the plane. The flow depth is typically increased upstream of a circular or square cylinder with the maximum flow depth occurring on the cylinder boundary at the upstream stagnation point, $\theta = \pi$. There is a decrease in flow depth downstream of the cylinder and the minimum flow depth occurs on the cylinder boundary at $\theta = 0$.

The magnitude of the perturbation to the flow depth is dependent upon a single dimensionless parameter, $\mathcal{F} = H_{\infty}/(L \tan \beta)$, which is the upstream flow depth divided by the product of the cylinder radius and the slope gradient (for noncircular cross-sections, L is a representative

lengthscale). For $\mathcal{F} \gg 1$, the perturbation is small. When $\mathcal{F} \ll 1$, however, the flow depth increases significantly upstream of the cylinder and dry regions in which there is no liquid occur downstream of the cylinder. We have also identified that the relatively deep region upstream of the cylinder is a pond of liquid with a horizontal free surface and the liquid is nearly stationary there. We have presented a numerical method that accurately determines the steady flow thickness past cylinders for a variety of cross-sections and a wide range of values of \mathcal{F} . The results demonstrate that the perturbation to the flow thickness is approximately antisymmetric about $x = 0$ in the case of a relatively narrow cylinder ($\mathcal{F} \gg 1$). For much wider cylinders ($\mathcal{F} \ll 1$), the numerical method enables the shape of the downstream dry region to be determined and illustrates the ponding upstream of the cylinder.

In the case of a circular cylinder, we have employed asymptotic analysis to expost the behavior of the flow in the regimes of wide ($\mathcal{F} \ll 1$) and narrow ($\mathcal{F} \gg 1$) cylinders. For a narrow cylinder, we have obtained a composite asymptotic approximation for the depth, which is accurate everywhere. For wide cylinders, we have quantified the significant increase in depth upstream of the cylinder in the ponded region. We have also found a simple empirical expression, $h_{\max} = (1 + 4\mathcal{F}^{-1})^{1/4}$, which provides a good approximation for the maximum flow depth for any value of \mathcal{F} .

We have extended the wide obstruction analysis to cylinders with square and wedge-shaped cross-section, which also have upstream ponds. The scaling for the flow depth upstream of a square cylinder is larger than for wedge and circular cylinders. The difference between the scaling for the flow depth is associated with the curvature of the upstream boundary of the obstruction. In the case of positive curvature on the upstream boundary (e.g., a wedge or circle), the flux into the pond is balanced by the component of gravity in the downslope direction. In the case of vanishing curvature (e.g., a square), there is no downslope flow out of the pond and the flux into the pond is balanced by the flux acting in the cross-slope direction associated with gradients of hydrostatic pressure. This flux is much smaller, for a fixed value of the flow depth, than the downslope flux in the regime of small \mathcal{F} and so the pond has a greater depth. We have also shown that for a wedge-shaped obstruction, the maximum flow depth occurs along the upstream wedge wall away from the stagnation point, in contrast to the square and circular cylinders. In the case of negative curvature (i.e. a concave obstruction), the scaling for the depth will be the same as the square cylinder because the oncoming flux is balanced by the cross-slope flux in the pond.

We also report new laboratory experiments with circular cylinders for a variety of slope angles, cylinder radii and oncoming flow thicknesses. The minimum and maximum thickness and the thickness along the centerline of the steady flow were measured nonintrusively by projecting a laser line onto the flowing surface. The results show very good agreement with our theoretical predictions and confirm the existence of dry regions downstream of obstructions in the case of a wide cylinder.

Our study was in part motivated by the need to inform the design of large-scale barriers that divert lava flows. The regime of a wide cylinder pertains to this context. The dry regions that occur downstream of obstructions provide safe zones for people, infrastructure and homes. However, barriers must also be constructed high enough to prevent overtopping and our calculations reveal the significant increase in flow heights that may be attained when $\mathcal{F} \ll 1$. Additionally, the barrier must be designed to withstand the force exerted on it by the flow and the calculation of which is also possible from our theory.

We have applied our asymptotic analysis to obtain approximations of the maximum flow depth on obstructions and demonstrated how this depends on the oncoming flow depth and the shape of the obstruction. We have also calculated the force exerted on an obstruction by the pond of liquid upstream formed when $\mathcal{F} \ll 1$. These results demonstrate that although a square obstruction may have a much larger dry region (thus protecting a greater area) than a circular obstruction, the square obstruction must be higher because it leads to a stronger increase in flow depth upstream. Furthermore, the square obstruction must also be able to withstand a much greater force. The results illustrate that the dependence of the extent and the shape of the dry region on the shape of the downstream side of the barrier is an important problem, and results are reported in Ref. [61].

ACKNOWLEDGMENTS

The authors gratefully acknowledge C. Gladstone, A. Pluck, and A. W. Woods for their assistance and advice with the laboratory experiments. They also acknowledge many interesting and stimulating discussions with K. Cashman, H. Dietterich, J. R. Lister, and A. Rust and with participants at the 2018 Woods Hole Oceanographic Institution's Geophysical Fluid Dynamics programme, which is supported by the National Science Foundation (Award No. 1332750).

 APPENDIX A: MATCHING IN THE REGIME $\mathcal{F} \gg 1$

In this Appendix, we match the inner solution Eq. (14) as $r \rightarrow \infty$ with the outer solution Eq. (31) as $\hat{r} \rightarrow 0$ to determine the correct form of the two expansions in Sec. IV for the regime $\mathcal{F} \gg 1$. We recall that the inner expansion is

$$h = 1 - \frac{\cos \theta}{r\mathcal{F}} + \mathcal{F}^{-2} \left[B_0 - \frac{3}{2} \log(r) - \frac{3}{4} \cos 2\theta - \frac{3}{4} r^{-2} \right]. \quad (\text{A1})$$

We match using an intermediate variable,

$$\rho = r\mathcal{F}^{-\alpha} = \hat{r}\mathcal{F}^{1-\alpha}, \quad (\text{A2})$$

with ρ fixed as $\mathcal{F} \rightarrow \infty$ and α between 0 and 1. In terms of the intermediate variable, the inner expansion is

$$h = 1 - \mathcal{F}^{-\alpha-1} \rho^{-1} \cos \theta + \mathcal{F}^{-2} \left[B_0 - (3/2) \log(\mathcal{F}^\alpha \rho) - (3/4) \cos 2\theta - \frac{3}{4} \mathcal{F}^{-2\alpha} \rho^{-2} \right] + \dots \quad (\text{A3})$$

The behavior of the modified Bessel functions, K_m , which occur in the outer expansion, as $\hat{r} \rightarrow 0$, are given by

$$K_0(3\hat{r}/2) \sim -\log(3\hat{r}/4) - \gamma \quad \text{and} \quad K_m(3\hat{r}/2) \sim [(m-1)!/2](3\hat{r}/4)^{-m}, \quad (\text{A4})$$

where $\gamma \approx 0.577$ is the Euler constant. In terms of the intermediate variable, the behavior is $K_m \sim \rho^{-m} \mathcal{F}^{m(1-\alpha)}$. The size of the terms in the sum in the outer expansion Eq. (31) increases with m and these cannot all be matched to the inner expansion Eq. (A3). We hence determine that $a_m = 0$ for $m \geq 2$. The outer expansion in the intermediate region is

$$h = 1 + \delta[-a_0\gamma - a_0 \log(3\mathcal{F}^{\alpha-1}\rho/4) + (2/3)\mathcal{F}^{1-\alpha}a_1\rho^{-1} \cos \theta][1 + (3/2)\mathcal{F}^{\alpha-1}\rho \cos \theta]. \quad (\text{A5})$$

The leading-order term of both inner and outer expansions is 1 and the next term in the inner expansion Eq. (A3) is $\mathcal{O}(\mathcal{F}^{-1-\alpha})$. The second order term in the outer expansion Eq. (A5) arises from K_1 and is $\mathcal{O}(\delta\mathcal{F}^{1-\alpha})$. To match the two expansions, we therefore choose

$$\delta = \mathcal{F}^{-2}. \quad (\text{A6})$$

At $\mathcal{O}(\mathcal{F}^{-1-\alpha})$, matching implies that

$$a_1 = -3/2. \quad (\text{A7})$$

At $\mathcal{O}(\mathcal{F}^{-2})$, we find that

$$-a_0 \log\left(\frac{3}{4}\right) - \gamma a_0 - a_0 \log(\rho) - a_0(\alpha-1) \log(\mathcal{F}) + \frac{a_1}{2} = B_0 - \frac{3}{2}\alpha \log(\mathcal{F}) - \frac{3}{2} \log(\rho). \quad (\text{A8})$$

Comparing $\log \rho$ terms and constant terms, we obtain

$$a_0 = \frac{3}{2}, \quad B_0 = -\frac{3}{2} \log\left(\frac{3}{4\mathcal{F}}\right) - \frac{3\gamma}{2} - \frac{3}{4}, \quad (\text{A9})$$

respectively. The inner and outer expansions are now fully determined up to order \mathcal{F}^{-2} .

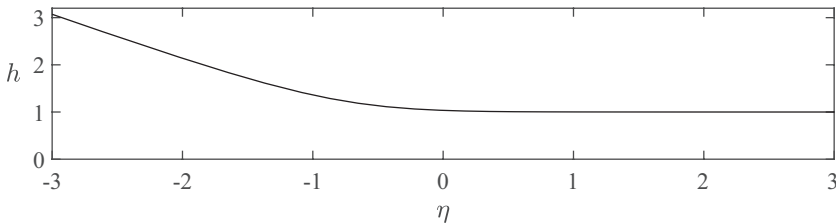


FIG. 18. Flow depth in the interior region of our asymptotic analysis, according to Eq. (B2).

APPENDIX B: MATCHING IN THE INTERIOR REGION TO DETERMINE $G(\theta)$

At the edge of the pond region (for the regime $\mathcal{F} \ll 1$), there is a region in which the flow depth returns to order 1. In the present section, we match through this interior region to obtain the form of the undetermined function, $G(\theta)$. In Sec. V, the scaling for this region was found to be

$$s = s_*(\theta) + \mathcal{F}^{1/4}\eta. \quad (\text{B1})$$

The leading-order governing partial differential equation in the interior region is

$$\cos\theta \frac{\partial h^3}{\partial \eta} = \frac{1}{4} \frac{\partial^2 h^4}{\partial \eta^2}, \quad (\text{B2})$$

with boundary conditions arising from the depth upstream ($\eta \rightarrow \infty$) and the depth in the pond ($\eta \rightarrow -\infty$),

$$h \rightarrow 1 \quad \text{as} \quad \eta \rightarrow \infty, \quad (\text{B3})$$

$$h \rightarrow \eta \cos\theta + \frac{k_{-2}(\theta)}{\eta^2 \cos^2\theta} \quad \text{as} \quad \eta \rightarrow -\infty. \quad (\text{B4})$$

We integrate the interior governing Eq. (B2) to obtain

$$\cos\theta(h^3 - 1) = h^3 \frac{\partial h}{\partial \eta}, \quad (\text{B5})$$

where we have used the condition Eq. (B3). We calculated the solution to Eq. (B5), with boundary condition Eq. (B4), numerically and it is shown in Fig. 18. As $\eta \rightarrow -\infty$, $h \rightarrow \eta \cos\theta$, which leads to

$$\frac{\partial h}{\partial \eta} = \cos\theta(1 - h^{-3}) \sim \cos\theta[1 - (\eta \cos\theta)^{-3}] \quad (\text{B6})$$

as $\eta \rightarrow -\infty$. We can compare this to Eq. (B4) to obtain

$$k_{-2}(\theta) = 1/2. \quad (\text{B7})$$

Then Eq. (48a) provides a differential equation for $G(\theta)$, which upon integrating becomes

$$G^4 \tan\theta = -4 \sin\theta + K. \quad (\text{B8})$$

The function $G(\theta)$ is bounded at $\theta = \pi$; thus, $K = 0$. The solution is

$$G(\theta) = (-4 \cos\theta)^{1/4}. \quad (\text{B9})$$

APPENDIX C: MATCHING AT HIGHER ORDER TO DETERMINE $k_0(\theta)$

In Sec. V, we found an asymptotic approximation for the flow thickness upstream of a circular cylinder in the regime of a wide cylinder ($\mathcal{F} \ll 1$). The maximum flow thickness occurs at $\theta = \pi$,

$r = 1$ and we found that the second order contribution to this thickness included $k_0(\pi)$, which was undetermined. In this Appendix, we match through the interior region at higher order to obtain an ordinary differential equation for $k_0(\theta)$, which we use to determine $k_0(\pi)$.

In the inner region, in which $r = 1 + \mathcal{F}^{3/4}s$, we found in Sec. V that the asymptotic approximation for the depth takes the form

$$h = \mathcal{F}^{-1/4}\mathcal{H}_0 + \mathcal{F}^{1/2}\mathcal{H}_1 + \mathcal{F}^{5/4}\mathcal{H}_2 + \dots \quad (\text{C1})$$

and by substituting into the governing Eq. (41), we obtain

$$\mathcal{H}_0 = s \cos \theta + G(\theta), \quad (\text{C2})$$

$$\mathcal{H}_1 = k_{-2}(\theta)\mathcal{H}_0^{-2} + k_0(\theta) + k_1(\theta)\mathcal{H}_0 + k_2(\theta)\mathcal{H}_0^2, \quad (\text{C3})$$

$$\mathcal{H}_2 = L_{-5}(\theta)\mathcal{H}_0^{-5} + L_{-3}(\theta)\mathcal{H}_0^{-3} + L_{-2}(\theta)\mathcal{H}_0^{-2} + \dots, \quad (\text{C4})$$

where $k_0(\theta)$ is to be determined and the other $k_i(\theta)$ are given in Eqs. (48a)–(48c). With $G(\theta)$ known Eq. (B9), these functions may be simplified to

$$k_{-2}(\theta) = 1/2, \quad (\text{C5})$$

$$k_1(\theta) = \frac{-3 \sin^2 \theta}{4 \cos^3 \theta} G(\theta), \quad (\text{C6})$$

$$k_2(\theta) = \frac{3 \tan^2 \theta - 1}{8 \cos \theta}. \quad (\text{C7})$$

Finally, the functions in \mathcal{H}_2 are found to be

$$L_{-5}(\theta) = -3/10, \quad (\text{C8})$$

$$L_{-3}(\theta) = -k_0(\theta), \quad (\text{C9})$$

$$L_{-2}(\theta) = [-2 \cos \theta]^{-1} [(k_0 G^3 \tan \theta)' + (17/20)G + (51/16)G \tan^2 \theta + (11/80)G \tan^4 \theta], \quad (\text{C10})$$

where in the last line we have suppressed the argument in $k_0(\theta)$ and $G(\theta)$ for brevity and $'$ denotes the derivative with respect to θ .

In Sec. V, we found an interior layer near $s = s^* = -G(\theta)/\cos \theta$, in which the thickness is order unity and we defined the coordinate

$$\eta = \mathcal{F}^{-1/4} \frac{G(\theta)}{\cos \theta} + \mathcal{F}^{-1}(r - 1). \quad (\text{C11})$$

Within this region, we transform from (r, θ) to (η, θ) coordinates and the governing Eq. (41) is recast as

$$\cos \theta \frac{\partial h^3}{\partial \eta} - \mathcal{F}^{3/4}(3/4) \tan^2 \theta G(\theta) \frac{\partial h^3}{\partial \eta} = \frac{\partial^2 h^4 / 4}{\partial \eta^2} + \mathcal{O}(\mathcal{F}). \quad (\text{C12})$$

As $\eta \rightarrow -\infty$, the thickness $h(\eta, \theta)$ is required to match with the approximation in which $s = \mathcal{O}(1)$ [Eq. (C1)]. We substitute for r in Eq. (C1) to obtain

$$\begin{aligned} h \sim & \eta \cos \theta + (1/2)(\eta \cos \theta)^{-2} - (3/10)(\eta \cos \theta)^{-5} + \mathcal{F}^{1/2} k_0(\theta) [1 - (\eta \cos \theta)^{-3}] \\ & + \mathcal{F}^{3/4} [k_1(\theta) \eta \cos \theta + L_{-2}(\theta) (\eta \cos \theta)^{-2}]. \end{aligned} \quad (\text{C13})$$

Thus, the expansion for h in the interior layer takes the following form:

$$h = h_0 + \mathcal{F}^{1/2} h_{1/2} + \mathcal{F}^{3/4} h_{3/4} + \dots \quad (\text{C14})$$

Substituting this expression into Eq. (C12), we obtain at $\mathcal{O}(\mathcal{F}^{3/4})$,

$$\cos \theta \frac{\partial}{\partial \eta} (3h_0^2 h_{3/4}) - \frac{3}{4} \tan^2 \theta G(\theta) \frac{\partial h_0^3}{\partial \eta} = \frac{\partial^2}{\partial \eta^2} (h_0^3 h_{3/4}). \quad (\text{C15})$$

Away from the cylinder, the depth returns to its unperturbed value and hence $h_0 \rightarrow 1$ and $h_{3/4} \rightarrow 0$ as $\eta \rightarrow \infty$. We integrate Eq. (C15) and apply this boundary condition to obtain

$$\frac{\partial h_{3/4}}{\partial \eta} = -\frac{3}{4} \tan^2 \theta G(\theta) (1 - h_0^{-3}) + \frac{3h_{3/4}}{h_0} \left(\cos \theta - \frac{\partial h_0}{\partial \eta} \right). \quad (\text{C16})$$

We apply our expressions for h_0 and $h_{3/4}$ as $\eta \rightarrow -\infty$ [Eq. (C13)] and compare the coefficients of η^{-3} to obtain

$$-2 \cos \theta l_{-2}(\theta) = -(3/4)G(\theta) \tan^2 \theta. \quad (\text{C17})$$

On substituting for $l_{-2}(\theta)$ from Eq. (C10), this is a first-order ordinary differential equation for $k_0(\theta)$ and by analyzing the behavior near $\theta = \pi$, we find that

$$k_0(\pi) = -17/40. \quad (\text{C18})$$

-
- [1] G. K. Batchelor, *An Introduction to Fluid Dynamics* (Cambridge University Press, Cambridge, UK, 1965).
 - [2] L. E. Stillwagon and R. G. Larson, Fundamentals of topographic substrate leveling, *J. Appl. Phys.* **63**, 5251 (1988).
 - [3] S. Kalliadasis, C. Bielarz, and G. Homsy, Steady free-surface thin film flows over topography, *Phys. Fluids* **12**, 1889 (2000).
 - [4] A. Mazouchi and G. Homsy, Free-surface Stokes flow over topography, *Phys. Fluids* **13**, 2751 (2001).
 - [5] M. G. Blyth and C. Pozrikidis, Film flow down an inclined plane over a three-dimensional obstacle, *Phys. Fluids* **18**, 052104 (2006).
 - [6] M. Sellier, Y. Lee, H. Thompson, and P. Gaskell, Thin film flow on surfaces containing arbitrary occlusions, *Comput. Fluids* **38**, 171 (2009).
 - [7] M. Sellier, Modeling the wetting of a solid occlusion by a liquid film, *Int. J. Multiphase Flow* **71**, 66 (2015).
 - [8] C. Pozrikidis, The flow of a liquid film along a periodic wall, *J. Fluid Mech.* **188**, 275 (1988).
 - [9] N. Malamataris and V. Bontozoglou, Computer aided analysis of viscous film flow along an inclined wavy wall, *J. Comput. Phys.* **154**, 372 (1999).
 - [10] M. Hayes, S. O'Brien, and J. Lammers, Green's function for steady flow over a small two-dimensional topography, *Phys. Fluids* **12**, 2845 (2000).
 - [11] Y. Lee, H. Thompson, and P. Gaskell, An efficient adaptive multigrid algorithm for predicting thin film flow on surfaces containing localised topographic features, *Comput. Fluids* **36**, 838 (2007).
 - [12] M. Schörner, D. Reck, and N. Aksel, Stability phenomena far beyond the Nusselt flow—Revealed by experimental asymptotics, *Phys. Fluids* **28**, 022102 (2016).
 - [13] P. Gaskell, P. Jimack, M. Sellier, H. Thompson, and M. Wilson, Gravity-driven flow of continuous thin liquid films on nonporous substrates with topography, *J. Fluid Mech.* **509**, 253 (2004).
 - [14] N. Aksel and M. Schörner, Films over topography: From creeping flow to linear stability, theory, and experiments, a review, *Acta Mech.* **229**, 1453 (2018).
 - [15] C. Heining and N. Aksel, Bottom reconstruction in thin-film flow over topography: Steady solution and linear stability, *Phys. Fluids* **21**, 083605 (2009).
 - [16] C. Heining, M. Sellier, and N. Aksel, The inverse problem in creeping film flows, *Acta Mech.* **223**, 841 (2012).
 - [17] S. J. Baxter, H. Power, K. A. Cliffe, and S. Hibberd, Three-dimensional thin film flow over and around an obstacle on an inclined plane, *Phys. Fluids* **21**, 032102 (2009).

- [18] E. M. Hinton, A. J. Hogg, and H. E. Huppert, Interaction of viscous free-surface flows with topography, *J. Fluid Mech.* **876**, 912 (2019).
- [19] G. I. Taylor and D. H. Michael, On making holes in a sheet of fluid, *J. Fluid Mech.* **58**, 625 (1973).
- [20] S. D. R. Wilson, The stability of a dry patch on a wetted wall, *Int. J. Heat Mass Transf.* **17**, 1607 (1974).
- [21] H. E. Huppert, Flow and instability of a viscous current down a slope, *Nature* **300**, 427 (1982).
- [22] T. Podgorski, J.-M. Flesselles, and L. Limat, Dry arches within flowing films, *Phys. Fluids* **11**, 845 (1999).
- [23] S. K. Wilson, B. R. Duffy, and S. H. Davis, On a slender dry patch in a liquid film draining under gravity down an inclined plane, *Eur. J. Appl. Math.* **12**, 233 (2001).
- [24] E. Rio and L. Limat, Wetting hysteresis of a dry patch left inside a flowing film, *Phys. Fluids* **18**, 032102 (2006).
- [25] J. Sébilleau, L. Lebon, and L. Limat, Stability of a dry patch in a viscous flowing film, *Eur. Phys. J.: Spec. Top.* **166**, 139 (2009).
- [26] Y. M. Yatim, B. R. Duffy, and S. K. Wilson, Travelling-wave similarity solutions for a steadily translating slender dry patch in a thin fluid film, *Phys. Fluids* **25**, 052103 (2013).
- [27] F. Barberi and M. L. Carapezza, *The Control of Lava Flows at Mt. Etna* (American Geophysical Union, Washington, DC, 2004), pp. 357–369.
- [28] R. W. Griffiths, The dynamics of lava flows, *Annu. Rev. Fluid Mech.* **32**, 477 (2001).
- [29] R. C. Kerr, R. W. Griffiths, and K. V. Cashman, Formation of channelized lava flows on an unconfined slope, *J. Geophys. Res.: Solid Earth* **111**, 1 (2006).
- [30] H. E. Huppert, J. B. Shepherd, R. H. Sigurdsson, and S. J. Sparks, On lava dome growth, with application to the 1979 lava extrusion of the Soufriere of St. Vincent, *J. Volcanol. Geotherm. Res.* **14**, 199 (1982).
- [31] R. S. J. Sparks and H. E. Huppert, Density changes during the fractional crystallization of basaltic magmas: Fluid dynamic implications, *Contrib. Mineral. Petrol.* **85**, 300 (1984).
- [32] P. C. Smith, A similarity solution for slow viscous flow down an inclined plane, *J. Fluid Mech.* **58**, 275 (1973).
- [33] J. R. Lister, Viscous flows down an inclined plane from point and line sources, *J. Fluid Mech.* **242**, 631 (1992).
- [34] B. R. Duffy and H. K. Moffatt, A similarity solution for viscous source flow on a vertical plane, *Eur. J. Appl. Math.* **8**, 37 (1997).
- [35] Z. P. Younger, G. A. Valentine, and T. K. Gregg, ‘A’ā lava emplacement and the significance of rafted pyroclastic material: Marcath volcano (Nevada, USA), *Bull. Volcanol.* **81**, 50 (2019).
- [36] H. J. Moore, *A Geologic Evaluation of Proposed Lava Diversion Barriers for the NOAA Mauna Loa Observatory Mauna Loa Volcano, Hawaii*, U.S. Geol. Surv. Open-File Report 82-314 (1982), pp. 1–26.
- [37] H. R. Dietterich, K. V. Cashman, A. C. Rust, and E. Lev, Diverting lava flows in the lab, *Nat. Geosci.* **8**, 494 (2015).
- [38] K. M. Hákonardóttir, A. J. Hogg, J. Batey, and A. W. Woods, Flying avalanches, *Geophys. Res. Lett.* **30**, 2191 (2003).
- [39] K. M. Hákonardóttir and A. J. Hogg, Oblique shocks in rapid granular flows, *Phys. Fluids* **17**, 077101 (2005).
- [40] X. Cui and J. Gray, Gravity-driven granular free-surface flow around a circular cylinder, *J. Fluid Mech.* **720**, 314 (2013).
- [41] T. Jóhannesson, P. Gauer, D. Issler, and K. Lied, *The Design of Avalanche Protection Dams. Recent Practical and Theoretical Developments*. European Commission, Directorate-General for Research, Publication EUR 23339 (2009).
- [42] M. O. Chevrel, A. Harris, A. Ajas, J. Biren, L. Gurioli, and L. Calabrò, Investigating physical and thermal interactions between lava and trees: the case of Kilauea’s July 1974 flow, *Bull. Volcanol.* **81**, 6 (2019).
- [43] N. Bernabeu, P. Saramito, and A. Harris, Laminar shallow viscoplastic fluid flowing through an array of vertical obstacles, *J. Non-Newtonian Fluid Mech.* **257**, 59 (2018).
- [44] H. E. Huppert and A. W. Woods, Gravity-driven flows in porous layers, *J. Fluid Mech.* **292**, 55 (1995).
- [45] Z. Zheng, L. Rongy, and H. A. Stone, Viscous fluid injection into a confined channel, *Phys. Fluids* **27**, 062105 (2015).

- [46] E. M. Hinton and A. W. Woods, Buoyancy-driven flow in a confined aquifer with a vertical gradient of permeability, *J. Fluid Mech.* **848**, 411 (2018).
- [47] W. Nusselt, Die Oberflächenkondensation des Wasserdampfes, VDI-Zs, Zeitschrift des Vereins Dtsch **60**, 541 (1916).
- [48] B. W. Thompson, Secondary flow in a Hele-Shaw cell, *J. Fluid Mech.* **31**, 379 (1968).
- [49] T. F. Balsa, Secondary flow in a Hele-Shaw cell, *J. Fluid Mech.* **372**, 25 (1998).
- [50] M. P. Dalwadi, S. J. Chapman, S. L. Waters, and J. M. Oliver, On the boundary layer structure near a highly permeable porous interface, *J. Fluid Mech.* **798**, 88 (2016).
- [51] M. P. Dalwadi, S. J. Chapman, J. M. Oliver, and S. L. Waters, The effect of weak inertia in rotating high-aspect-ratio vessel bioreactors, *J. Fluid Mech.* **835**, 674 (2018).
- [52] E. J. Hinch, *Perturbation Methods*. Cambridge texts in applied mathematics (Cambridge University Press, Cambridge, UK, 1991).
- [53] I. Proudman and J. R. A. Pearson, Expansions at small Reynolds numbers for the flow past a sphere and a circular cylinder, *J. Fluid Mech.* **2**, 237 (1957).
- [54] M. Abramowitz and I. A. Stegun, *Handbook of Mathematical Functions with Formulas, Graphs and Mathematical Tables*. Dover books on intermediate and advanced mathematics (Dover, New York, 1965).
- [55] J. R. Lister, Slow Viscous Flow Examination Paper, Part III of the Cambridge Mathematical Tripos. (2016).
- [56] D. R. Hewitt and N. J. Balmforth, Thixotropic gravity currents, *J. Fluid Mech.* **727**, 56 (2013).
- [57] T.-F. Dauck, F. Box, L. Gell, J. A. Neufeld, and J. R. Lister, Shock formation in two-layer equal-density viscous gravity currents, *J. Fluid Mech.* **863**, 730 (2019).
- [58] D. Pihler-Puzović, A. Juel, G. G. Peng, J. R. Lister, and M. Heil, Displacement flows under elastic membranes. Part 1. Experiments and direct numerical simulations, *J. Fluid Mech.* **784**, 487 (2015).
- [59] T. V. Ball and J. A. Neufeld, Static and dynamic fluid-driven fracturing of adhered elastica, *Phys. Rev. Fluids* **3**, 074101 (2018).
- [60] E. W. Llewellyn, H. M. Mader, and S. D. R. Wilson, The rheology of a bubbly liquid, *Proc. R. Soc. London A* **458**, 987 (2002).
- [61] E. M. Hinton, A. J. Hogg, and H. E. Huppert, Shallow free-surface Stokes flow around a corner, *Philos. Trans. R. Soc. London A* **378**, 20190515 (2020).